Middle Jurassic MORB-type gabbro, high-Mg diorite, calc-alkaline diorite and granodiorite in the Ando area, central Tibet: Evidence for a slab roll-back of the Bangong-Nujiang Ocean

Haoyu Yan [a,b], Xiaoping Long [c,*], Xuan-Ce Wang [d], Jie Li [a], Qiang Wang [a], Chao Yuan [a], Min Sun [e]

[a] State Key Laboratory of Isotope Geochemistry, Guangzhou Institute of Geochemistry, Chinese Academy of Sciences, Guangzhou 510640, China
[b] University of Chinese Academy of Sciences, Beijing 10069, China
[c] State Key Laboratory of Continental Dynamics, Department of Geology, Northwest University, Xi'an 710069, China
[d] The Institute for Geoscience Research (TIGeR), Department of Applied Geology, Curtin University of Technology, Perth, WA 6845, Australia
[e] Department of Earth Sciences, The University of Hong Kong, Pokfulam Road, Hong Kong, China

ARTICLE INFO

ABSTRACT

Mesozoic intrusions, including MORB-type gabbros, high-Mg diorites, calc-alkaline diorites and granodiorites, were exposed in the Ando microcontinent that is bounded between the Qiangtang and Lhasa terranes. Discoveries of these Mesozoic intrusions have provided new petrogenetic constraints on our understanding of Bangong-Nujiang ocean evolution. Zircon U–Pb dating shows that these intrusions formed in the early-middle Jurassic (174–177 Ma). The gabbros have relatively flat REE distribution patterns, which is analogous to the geochemical features of MORB. Their positive $\varepsilon_{Nd}(t)$ values ($\varepsilon_{Nd}(t) = 4.4$–5.5) are consistent with those of ophiolites along the Bangong-Nujiang suture zone. These gabbros are also characterized by enrichments of fluid-sensitive elements and negative to positive Nb anomalies, indicative of the influence of subduction-related compositions in their mantle source. These features suggest that the gabbros were most likely originated from asthenosphere-derived melts metasomatized by enriched lithospheric mantle during the upwelling. The high-Mg diorites are characterized by typical features of high compatible elements (MgO = 8.3–10.24 wt%, Cr = 400–547 ppm, Ni = 120–152 ppm), high Mg# (70–74) and low Sr/Y ratios. Their high initial $^{87}Sr/^{86}Sr$ isotopic ratios and negative $\varepsilon_{Nd}(t)$ values (-10.5 to -10.8), together with their sanukitic characteristics, imply that the high-Mg diorites were probably produced by partial melting of mantle peridotites metasomatized by slab-derived melts and aqueous fluids. The calc-alkaline diorites have relatively high MgO (4.04–5.50 wt%), Cr, Ni contents and Mg# (56–59), as well as high $(^{86}Sr/^{87}Sr)_i$ ratios and negative $\varepsilon_{Nd}(t)$ values (-7.5 to -7.3), suggesting that they were most likely formed by partial melting of the Ando basement rocks with significant input of mantle components. The granodiorites are peraluminous and have higher $(^{86}Sr/^{87}Sr)_i$ ratios and more negative $\varepsilon_{Nd}(t)$ values (-10.6 to -10.8), similar to those of the granitic gneisses of the Ando basement, suggesting partial melting of the Ando basement. Taking into account the spatial and temporal distribution of the Mesozoic magmatic rocks in the Southern Qiangtang terrane, we suggest that the formation of the Early-Middle Jurassic magmatic "flare-up" in the Southern Qiangtang terrane was related to the asthenospheric upwelling triggered by the roll-back of the subducted Bangong–Nujiang oceanic slab.

1. Introduction

Magmatic rocks is crucial to investigate regional tectonic events and can provide further important constrains on deep geodynamic processes. The growth and reworking of continental crust is commonly triggered by the underplating of mantle magmas (Chen and Arakawa, 2005; Jahn et al., 2004). In subdution zones, the mantle rocks and the coeval granites have therefore recorded abundant information regarding the crustal growth and differentiation of continental crust (Kamei et al., 2004; Karsli et al., 2010). However, the production of the subdution-related magmatic rocks was always attributed to distinct dynamic mechanisms, including slab break-off (Davies and von Blanckenburg, 1995), ridge sub-duction (Abratis and Worner, 2001; Guivel et al., 1999), slab tearing (Guivel et al., 2006; Pallares et al., 2007), or slab roll-back (Kay and Mpodozis, 2001; Ramos and Folguera, 2009). All of these geodynamic processes are closely corresponding to the upwelling of hot astheno-sphere mantle, which provides enough heat for partial melting of the subducted oceanic crust and marine sediments, the overlying sub-continental lithospheric mantle and low crust. The partial melting of these unites always generates some distinct magmatic rocks in various

tectonic regimes, such as high-Mg andesite, adakite, which therefore can be used to constrain the different geodynamic processes.

The uplift of Tibetan Plateau is generally considered to have formed by continental collision between India and Eurasian along the Indus–Yarlung suture in the early Cenozoic (Chung et al., 2005; DeCelles et al., 2002; Ding et al., 2005; Nelson et al., 1996; Yin and Harrison, 2000). Recently, more and more evidence indicates that the pre-Cenozoic tectonics and magmatism probably contributed to the accretion and formation of the central and northern Tibetan Plateau before the final India and Eurasian collision (Guynn et al., 2012; Kapp et al., 2003, 2007; Long et al., 2015; Murphy et al., 1997; Pullen et al., 2011). For example, an active continental margin is proposed to have developed in the Southern Qiangtang caused by the subduction of the Bangong-Nujiang Ocean (BNO), which is predated to the collision between the Lhasa and Qiangtang terranes (Kapp et al., 2005; Liu et al., 2014). Late Mesozoic intermediate–felsic intrusions in the Southern Qiangtang terrane are considered to have been produced by the northward subduction of the Bangong–Nujiang Ocean (S.M. Li et al., 2014; J.X. Li et al., 2014; Pullen et al., 2011). Recently, early Jurassic granitoids (185–175 Ma) were discovered in the Ando microcontinent along the margin of the Southern Qiangtang terrane (Liu et al., 2011, 2015). These Mesozoic granitoids were suggested to represent a "missing" Jurassic continental arc along the Southern Qiangtang terrane (Guynn et al., 2006), but the detailed subduction processes related to the Bangong–Nujiang Ocean are still controversial. For example, the closure timing, the subduction polarity and the subduction-related tectonic model are poor constrained.

In order to constrain the tectonic setting and crustal growth in central Tibet, we present new zircon U–Pb ages, whole-rock geochemical and Sr-Nd isotopic data for Jurassic MORB-type gabbros, high-Mg diorites, calc-alkaline diorites and granodiorites in the Ando area. Based on the petrogenesis of these intrusions, a slab roll-back model of the subducted Bangong-Nujiang Ocean is proposed to interpret the tectonic regime when the Jurassic mafic-felsic intrusions formed.

2. Geological background

The central and southern Tibetan plateau is commonly divided into three terranes from south to north, including Lhasa, Qiangtang and Songpan-Ganze, which were separated by the Mesozoic Bangong–Nujiang and Jinshajiang suture zones, respectively (Fig. 1; Chung et al., 2005; Ding et al., 2007; Yin and Harrison, 2000). It is generally accepted that the Bangong–Nujiang ocean opened during the Permian–Triassic or Early Jurassic and closed prior to the Early Cretaceous (Murphy et al., 1997), whereas the formation of the Jinshajiang suture predates the Jurassic (Tapponnier et al., 2001). (See Fig. 2.)

The Bangong–Nujiang suture zones (BNSZ) extends more than 2000 km from west to east, which can be subdivided into the western (Bangong Lake-Gaize), the middle (Dongqiao-Amdo), and the eastern (Dingqing-Nujiang) sectors (Pan et al., 2012). The suture zone is made up of a discontinuous belt of flysch, mélange and ophiolitic fragments (Kapp et al., 2003; B.D. Wang et al., 2016; K.J. Zhang et al., 2014; X.Z. Zhang et al., 2014). To the south, the Lhasa terrane is divided into northern, central, and southern subterranes, based on basement rocks and
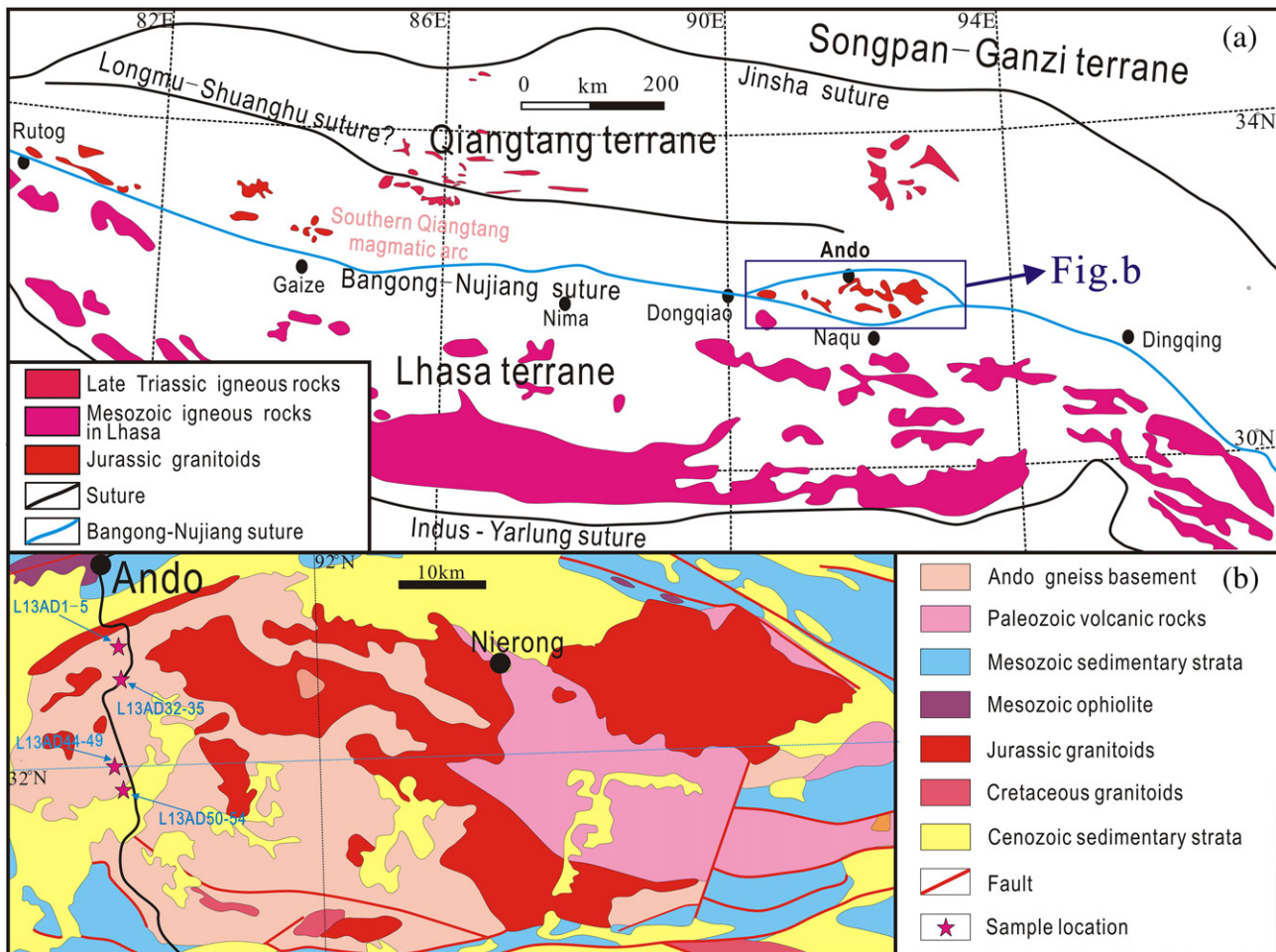

Fig. 1. (a) Tectonic map of the central and southern Tibet and geological map of the studied are From north to south: Songpan–Ganzi terrane, Jinsha suture, Northern Qiangtang terrane, Longmu-Shuanghu suture, Southern Qiangtang terrane, Bangong–Nujiang suture, Lhasa terrane, Indus-Yarlung suture (modified after Chen et al., 2016; Liu et al., 2015; Zhai et al., 2013). (b) Geological map of the Ando terrane (after BGTAR, 2005).
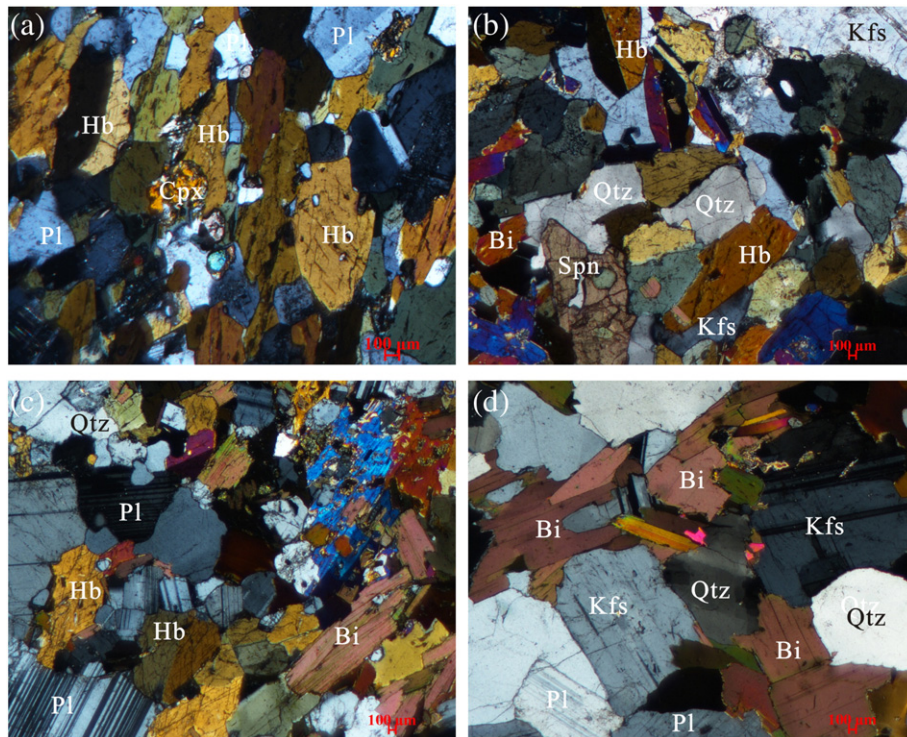
Fig. 2. Textural characteristics of the Jurassic plutons. Under cross-polarized light. (a) gabbro, (b) high-Mg diorite, (c) calc-alkaline diorite, (d) granodiorite. Pl = plagioclase. Hb = hornblende, Py = pyroxene, Kfs = K-feldspar, Bi = biotite, Spn = sphene, and Qtz = quartz.

sedimentary cover (Zhu et al., 2011). Differently, to the north of the BNSZ, some researchers recently suggested that the Qiangtang terrane was composed of two subterranes separated by the east–west-trending Longmu–Shuanghu suture (Li et al., 2006; Zhang et al., 2012; Zhu et al., 2013). The Longmu–Shuanghu suture is usually considered as a residue of an Ordovician–Triassic Paleo-Tethyan ocean (Liu et al., 2011; Yin and Harrison, 2000; Zhu et al., 2013). The ocean was suggested to have closed during the Triassic based on the presence of the Triassic high-pressure metamorphic rocks belt in the central Qiangtang (Zhai et al., 2011a, 2011b, 2013). However, Kapp et al. (2000, 2003) suggested that the Longmu–Shuanghu metamorphic rocks belt was only a metamorphic core complex produced by underthrusting of Jinshajiang ocean lithosphere beneath the Qiangtang Terrane during the Early Mesozoic, then to be exhumed in an intracontinental setting by Late Triassic–Early Jurassic normal faulting. Recently, Zeng et al. (2015) proposed that the exhumation of Triassic Qiangtang metamorphic event was due to the northward subduction of Bangong-Nujiang Ocean beneath the Qiangtang terrane during late Triassic.

The Ando terrane is an isolated microcontinent within the Bangong–Nujiang suture zone and bounded by Mesozoic ophiolites to its north and south sides (Guynn et al., 2006, 2012; Shi et al., 2012; K.J. Zhang et al., 2014; X.Z. Zhang et al., 2014; Zhu et al., 2013). The microcontinent consists mainly of orthogneisses with minor metasedimentary rocks, mafic amphibolites and migmatites, which were intruded by Jurassic granitoids (Kapp et al., 2005; Zhang et al., 2012; Zhu et al., 2011). Beside Nyainqêntanglha massif, the Ando microcontinent is the only one with well defined outcrops of Neoproterozoic (920–820 Ma) and Cambrian-Ordovician (540–460 Ma) crystalline basement in the interior of Tibet (Guynn et al., 2006; Kapp et al., 2005; Xu et al., 1985; Zhu et al., 2011).

Recently, abundant of Jurassic magmatic rocks were identified to occur along the southern margin of the Southern Qiangtang terrane, extending from the Bangong Co in the westernmost, through Gaize and Amdo in the middle, to Dingqing in the eastern (Guynn et al., 2006; S.M. Li et al., 2014; J.X. Li et al., 2014; Liu et al., 2014, 2015). These magmatic rocks were considered to be produced in a magmatic arc setting (Guynn et al., 2006; Zhang et al., 2012). In this study, MORB-type gabbros, high-Mg diorites, calc-alkaline diorites and grano-diorites were collected from the southern Ando microcontinent. All of these samples intruded into the Precambrian basement rocks (Fig. 1). The gabbros consist of plagioclase (~40 vol.%), hornblende (~50 vol.%), clinopyroxene (<10 vol.%) (Fig. 2a). The high-Mg diorites are mainly composed of plagioclase (~20 vol.%), K-feldspar(~25 vol.%), hornblende (~45 vol.%) and quartz (<10 vol.%), with minor accessory zircon, apatite, titanite and Fe–Ti oxides (Fig. 2b). The calc-alkaline diorites consist of plagioclase (~45 vol.%), hornblende (~35 vol.%) and biotite (~15 vol.%), with minor quartz (<5 vol.%) and accessory minerals (Fig. 2c). In contrast, the calc-alkaline granodiorites have more K-feldspar (~35 vol.%), biotite (~25 vol.%), quartz (~15 vol.%), but less plagioclase (~25 vol.%) (Fig. 2d). All of these samples are middle-grained without mafic enclaves.

3. Analytical methods

3.1. Major and trace elements

Fifteen samples (Fig. 1) were chosen for geochemical analysis and such analyses were carried out at the State Key Laboratory of Isotope Geochemistry (SKLIG), Guangzhou Institute of Geochemistry, Chinese Academy of Sciences (CAS). These sample were first crushed into small pieces, then ultrasonically cleaned in distilled water, and finally dried and powdered to 200 meshes. Major element oxides of whole-rock samples were determined by Rigaku ZSX100e X-ray fluorescence spectrometer. The detailed operating procedures are the same as those described by Chen et al. (2010). The analytical uncertainty of the XRF in this lab are generally between 1% and 5%. Trace elements, including the rare earth elements (REE), were analyzed by an inductively coupled plasma mass spectrometry (ICP-MS), using a Perkin-Elmer Sciex ELAN 6000 instrument at the same institute. Before geochemical analysis, the powdered samples (50 mg) were digested with mixed HNO_3 + HF acid in Teflon-coated steel bombs in order to assure complete dissolution of refractory minerals. A solution containing Rh

was used as internal standard to monitor the signal drift. Eight rock standards, including the USGS rock standards (G-2, W-2, MRG-1 and AGV-1) and the Chinese national rock standards (GSD-12, GSR-1, GSR-2 and GSR-3), were used to calibrate the elemental concentrations of our samples. The analytical precision for trace elements was generally better than 5% in this laboratory. Major and trace element results from those samples are listed in Table 1.

3.2. Zircon U–Pb dating

Four samples collected from the Ando plutons were selected for zircon LA-ICPMS U–Pb dating. The cathodoluminescence (CL) imaging was performed using a JXA-8100 Electron Probe Microanalyzer with a Mono CL3 Cathodoluminescence System in the Guangzhou Institute of Geochemistry to observe the internal structure of the zircons.

Zircon U–Pb dating was carried out using a LA-ICP-MS at the State laboratory in the same institute. The analytical description are divided into seven steps as described by Li et al. (2011): 1) Sample mounts were placed in a sample cell designed by Laurin Technic Pty. Ltd., flushed with Ar and He; 2) Laser ablation was performed using a pulsed Resonetic 193 nm ArF excimer laser, operated at a constant energy of 80 mJ, with a repetition rate of 8 Hz and a spot diameter of 31 μm; 3) The ablated aerosol was carried to an Agilent 7500a ICP-MS by He gas via a Squid system to smooth signals; 4) Data were acquired for 30 s with the laser off, and 40 s with the laser on, giving approximately 100 mass scans; 5) Each block of 5 unknowns was bracketed by analyses of external standards, including NIST SRM 610 glass and the Temora zircon; 6) Off-line data processing was performed using ICPMSDataCal (Liu et al., 2008); 7) The common Pb correction was carried out using the Excel program ComPbCorr#3 (Andersen, 2002). The Plesovice

Table 1
Geochemistry of the Ando magmatic rocks in the Southern Qiangtang terrane.

Sample	L13 AD51	L13 AD52	L13 AD53	L13 AD54	L13 AD33	L13 AD34	L13 AD35	L13 AD02	L13 AD03	L13 AD04	L13 AD05	L13 AD45	L13 AD46	L13 AD47	L13 AD48
Rock-type	Gabbro				High-Mg diorite			Cal-alkaline diorite				Granodiorite			
SiO_2	47.10	54.52	47.03	47.30	56.45	54.69	55.92	55.88	52.93	56.30	56.27	62.16	65.99	65.12	62.90
TiO_2	1.26	1.18	1.00	1.08	1.13	1.33	1.27	0.97	1.03	1.08	1.01	0.76	0.63	0.83	0.85
Al_2O_3	14.43	14.06	16.56	14.93	11.08	9.94	10.82	17.24	17.05	17.32	17.73	18.15	16.09	15.77	16.78
$Fe_2O_3^T$	11.86	10.95	11.26	11.66	8.02	7.96	7.41	7.40	8.74	7.26	7.21	5.60	4.60	6.02	6.34
MnO	0.20	0.20	0.21	0.18	0.17	0.17	0.15	0.13	0.18	0.12	0.13	0.06	0.05	0.07	0.06
MgO	7.24	4.84	7.19	7.88	8.30	10.24	9.09	4.77	5.50	4.46	4.04	2.15	1.81	2.32	2.46
CaO	13.75	8.79	11.99	12.13	6.05	8.00	6.80	6.77	7.51	6.40	6.64	3.63	2.02	2.85	3.04
Na_2O	2.20	2.99	1.97	2.47	1.15	1.32	1.23	3.22	3.10	3.15	3.35	3.56	2.48	2.86	3.10
K_2O	0.78	1.15	1.29	1.09	5.79	4.19	5.17	1.81	1.99	1.99	1.93	2.67	4.98	2.75	3.02
P_2O_5	0.11	0.10	0.09	0.10	0.29	0.30	0.30	0.17	0.18	0.17	0.17	0.06	0.06	0.06	0.08
LOI	0.63	0.78	0.98	0.77	1.13	1.42	1.40	1.22	1.36	1.32	1.09	0.76	0.86	0.92	0.94
Total	99.55	99.56	99.56	99.56	99.57	99.57	99.57	99.56	99.57	99.57	99.56	99.56	99.56	99.56	99.56
Na_2O/K_2O	2.83	2.59	1.52	2.27	0.2	0.31	0.24	1.78	1.56	1.59	1.74	1.33	0.5	1.04	1.03
A/CNK	0.49	0.63	0.63	0.55	0.58	0.47	0.54	0.88	0.81	0.91	0.9	1.18	1.22	1.22	1.21
$Mg^{\#}$	57.77	49.76	58.89	60.25	69.86	74.25	73.33	59.09	58.51	57.96	55.71	46.2	46.85	46.36	46.46
Sc	44.4	36.5	45.9	49.7	41.2	36.0	29.7	25.8	34.1	28.0	25.8	13.7	11.4	14.1	17.5
Cr	232	40.4	488	238	400	547	456	93.2	161	58.2	51.6	19.8	33.2	27.7	38.2
Co	49.3	34.7	48.5	53.9	31.5	39.7	34.5	25.4	29.9	23.7	23.2	12.3	10.6	13.4	15.2
Ni	89.4	39.1	144	92.3	120	152	131	35.4	43.2	22.0	21.9	15.6	19.5	19.4	25.2
Ga	17.6	22.8	16.7	16.7	17.8	17.1	17.4	20.6	20.6	19.8	20.0	25.0	19.4	22.8	28.2
Ge	2.86	2.69	2.78	2.65	3.72	3.63	3.14	1.83	2.01	1.75	1.75	2.60	1.90	2.50	3.13
Rb	17.6	32.9	42.7	16.0	323	211	331	89.4	91.1	102	95.1	208	245	218	267
Sr	107	86.7	101	95.8	187	178	215	300	283	283	300	227	225	179	220
Cs	1.64	1.73	2.83	0.79	8.63	4.21	8.72	3.97	3.10	5.38	6.04	14.2	11.0	14.0	16.8
Ba	33.7	43.1	57.7	23.5	1571	1061	1457	452	470	460	465	266	1591	282	340
La	4.13	4.67	3.86	2.75	32.23	59.7	65.9	31.4	23.1	18.5	18.9	60.7	21.8	52.5	67.9
Ce	11.0	12.8	10.6	7.92	98.5	135	138	69.0	71.9	45.5	48.1	116	40.8	98.8	130
Pr	1.76	2.11	1.58	1.34	16.4	18.7	17.5	8.84	9.52	6.02	6.64	13.7	4.61	11.15	15.4
Nd	9.28	10.9	8.16	7.31	71.2	72.5	61.1	35.6	42.2	25.0	28.7	47.8	16.4	39.4	54.0
Sm	3.13	4.11	2.68	2.55	15.7	11.9	9.04	7.65	10.3	5.52	6.68	9.36	3.03	7.12	10.2
Eu	1.05	1.05	0.89	0.92	2.33	2.19	1.58	1.54	1.85	1.31	1.46	1.57	1.28	1.27	1.56
Gd	3.63	5.05	3.03	3.04	12.0	8.50	6.78	7.11	9.96	5.22	6.63	9.10	2.73	6.10	9.21
Tb	0.75	1.14	0.62	0.66	1.99	1.05	0.75	1.16	1.65	0.85	1.10	1.53	0.40	0.85	1.36
Dy	5.10	7.88	4.17	4.62	11.48	4.95	3.34	7.07	10.2	5.30	6.74	9.25	2.27	3.96	6.95
Ho	1.13	1.71	0.92	1.04	2.31	0.95	0.64	1.41	2.07	1.08	1.33	1.91	0.47	0.68	1.30
Er	3.20	4.74	2.55	3.00	6.16	2.44	1.67	3.93	5.56	2.97	3.65	5.07	1.31	1.58	3.27
Tm	0.47	0.70	0.37	0.45	0.91	0.34	0.24	0.53	0.78	0.42	0.49	0.67	0.20	0.20	0.43
Yb	2.97	4.44	2.45	2.86	5.70	2.25	1.65	3.34	4.84	2.57	3.00	3.86	1.31	1.26	2.69
Lu	0.46	0.65	0.37	0.44	0.82	0.35	0.27	0.50	0.71	0.39	0.45	0.57	0.21	0.20	0.41
Y	28.2	44.5	22.4	25.5	57.5	23.1	14.1	40.1	58.2	30.3	37.7	49.1	11.2	15.0	31.9
Zr	62.5	80.3	51.0	47.5	309	393	383	154	143	93.6	184	178	228	225	270
Hf	2.02	2.66	1.56	1.54	9.29	11.1	10.7	3.98	4.04	2.55	4.62	4.90	6.25	6.28	7.77
Nb	5.54	16.6	4.00	2.44	24.7	16.9	12.9	10.5	11.8	9.96	9.99	15.4	12.1	15.7	19.8
Ta	1.27	2.13	0.36	0.18	3.31	0.78	0.78	1.07	1.30	1.17	1.23	1.69	1.25	1.70	2.19
Th	0.74	1.48	0.54	0.09	16.5	46.1	33.1	8.51	9.36	3.18	2.80	41.3	13.2	35.1	47.4
U	2.01	3.36	1.4	0.09	4.56	5.71	3.64	1.24	6.99	1.76	2.54	3.25	1.83	2.77	3.92
Pb	8.08	28.8	11.8	5.09	29.0	22.5	20.6	68.0	27.8	42.5	30.1	30.7	50.0	25.1	29.8
$(La/Yb)_N$	1.00	0.75	1.13	0.69	4.05	19.0	28.7	6.75	3.42	5.17	4.52	11.3	11.9	29.9	18.1
$(Gd/Yb)_N$	1.00	0.94	1.03	0.88	1.75	3.13	3.41	1.76	1.70	1.68	1.83	1.95	1.72	4.00	2.84
Eu/Eu^*	0.95	0.70	0.94	1.00	0.50	0.63	0.59	0.63	0.55	0.73	0.66	0.51	1.34	0.58	0.48

Note: The units of major and trace elements are wt.% and ppm, respectively. A/CNK = molar ratio of $Al_2O_3/(CaO + Na_2O + K_2O)$; $Mg^{\#}$ = molar ratio of $MgO/(MgO + 0.89*Fe_2O_3^T)*100$.

zircon was used as a secondary standard to check the accuracy of the analyses (Sláma et al., 2008). The analytical results are presented in Appendix Table S1.

3.3. Sr–Nd isotopes

Eight samples were analyzed for whole-rock Sr–Nd isotopic compositions using a MC-ICP-MS at the State laboratory in the CAS. Analytical procedures are described by Li et al. (2004). Sample powders (50–100 mg) were digested with distilled HF-HNO$_3$ in screw-top PFA beakers at 120 °C for 7 days. Sr and REEs were then separated using cation columns and Nd fraction were further separated with HDEHP columns. The $^{87}Sr/^{87}Sr$ and $^{143}Nd/^{144}Nd$ ratios of the JNdi-1 standard material were measured during this study and all the measured $^{87}Sr/^{87}Sr$ and $^{143}Nd/^{144}Nd$ ratios were corrected for fractionation to $^{86}Sr/^{88}Sr = 0.1194$ and $^{146}Nd/^{144}Nd = 0.7219$, respectively. The Sr–Nd isotopic results are listed in Table 2.

4. Results

4.1. Zircon U–Pb ages

Zircon grains from the studied samples are euhedral to subhedral with prismatic or granular shapes and crystal lengths of 95–180 μm. The CL images of zircons show oscillatory growth zoning and Th/U ratios of 0.28–2.5 > 0.1, indicating a magmatic origin (Corfu et al., 2003).

Twenty-five zircon grains from a gabbro sample (L13 AD50) were analyzed and yielded similar $^{206}Pb/^{238}U$ ages between 171 Ma and 183 Ma, with a weighted mean age of 176.6 ± 0.8 Ma (MSWD = 1.6) (Fig. 3a and Appendix Table S1), representing the crystallization age. Twenty-five zircons from a high-Mg diorite sample (L13 AD32) were dated for U–Pb ages. Their $^{206}Pb/^{238}U$ ages range from 168 Ma to 178 Ma, yielding a weighted mean age of 173.7 ± 1.2 Ma (MSWD = 0.66) (Fig. 3b). This mean age is interpreted as the crystallization age of the high-Mg diorite rocks. Thirty analyses on zircons from a calc-alkaline diorite sample (L13 AD01) yielded $^{206}Pb/^{238}U$ ages ranging from 169 Ma to 185 Ma and a weighted mean age of 174.8 ± 1.2 Ma (MSWD = 1.12), representing the crystallization age (Fig. 3c). Analyses on twenty-four grains from the calc-alkaline granodiorites sample (L13 AD44) yield two populations of U–Pb ages, One population generated a weight mean $^{206}Pb/^{238}U$ age of 177.4 ± 1.2 Ma (n = 16; MSWD = 0.78) (Fig. 3d), whereas the other population give much older $^{206}Pb/^{238}U$ ages varying from 734 Ma to 1771 Ma. The weight mean age of the younger population is interpreted to represent the

crystallization of sample L13 AD44, but the Precambrian population is interpreted as inherited zircon grains.

4.2. Major and trace elements

The gabbros mostly have SiO$_2$ contents varying from 47.03 wt.% to 47.30 wt.%, with relatively high MgO (7.19–7.88 wt.%), Al$_2$O$_3$ (14.43–16.56 wt.%) and TiO$_2$ (1.0–1.27 wt.%) (Table 1), but relatively low total alkali (Na$_2$O + K$_2$O = 2.98–3.55 wt.%). Sample L13 AD52, however, shows more evolved geochemical compositions (SiO$_2$ = 54.52 wt.%, TiO$_2$ = 1.18 wt.%, MgO = 4.84 wt.%, Na$_2$O + K$_2$O = 4.14 wt.%). The gabbro samples plot in the subalkaline fields in the TAS diagram (Fig. 4a and d), and define a typical tholeiitic trend in a SiO$_2$ versus FeO^{Total}/MgO diagram (Miyashiro, 1974) (not showing).

The gabbros have variable Cr (40–488 ppm) and Ni (39–144 ppm), and high Zr/Nb (253–837) and Nb/La (0.88–3.54) ratios. They are characterized by MORB-like REE patterns with relatively flat REE ([La/Yb]$_N$ = 0.70–1.13) but slightly negative Eu anomalies (δEu = 0.70–1.01) (Fig. 5a). The rocks have (La/Sm)$_N$ ratios ranging from 0.70 to 0.93 that are higher than N-MORB. On the primitive mantle-normalized diagram (Fig. 5b), they show enrichments in large ion lithophile elements (LILE, e.g., Pb, Rb and Ba) relative to the high field strength elements (HFSE, e.g., Nb and Ta).

The high-Mg diorites possess relatively high SiO$_2$ (54.69–56.45 wt.%) and TiO$_2$ (1.13–1.33 wt.%), but low Al$_2$O$_3$ (9.94–11.08 wt.%) contents. The samples are characterized by high MgO (8.30–10.24 wt.%), Mg$^{\#}$ (70–74), Cr (400–547 ppm) and Ni (120–152 ppm), but low CaO (6.05–8.00 wt.%) and FeO^{total}/MgO ratios (0.78–0.97). They all plotted in the field of high–Mg andesite (HMA) in the MgO versus SiO$_2$ diagram (Fig. 9a). The rocks have high K$_2$O (4.19–5.79 wt.%) and low Na$_2$O (1.15–1.32 wt.%), therefore with high K$_2$O/Na$_2$O ratios, showing shoshonitic series characteristics in the SiO$_2$ versus K$_2$O diagram (Fig. 4b). The high-Mg diorites display fractionated REE patterns characterized by various enrichments of LREE, slightly deletion of HREE ((La/Yb)$_N$ = 4.06–28.70; (Gd/Yb)$_N$ = 1.75–3.41), and weak negative Eu anomalies (δEu = 0.50–0.63) (Fig. 5c). They have low Sr (178–215 ppm) and Yb (1.60–5.70), high Y (14.1–57.5 ppm) and thus low Sr/Y (3.25–15.20) ratios. The samples are characterized by high Ba (1061–1571 ppm) and show significant enrichment in LILE (e.g., K, Rb, and Pb), and depletion in HFSE (e.g., Nb, Ta, and Ti) (Fig. 5d).

The calc-alkaline diorites have relatively lower SiO$_2$ (52.93–56.30 wt.%), MgO (4.04–5.50 wt.%), Mg$^{\#}$ (56–59), K$_2$O (1.81–1.99 wt.%) and TiO$_2$ (0.97–1.08) than the high-diorites, but with higher Al$_2$O$_3$ (17.05–17.73 wt.%) and Na$_2$O (3.10–3.35 wt.%) contents. The samples plot near the boundary of the gabbro and diorite and fall into subalkaline

Table 2
Sr–Nd isotopic composition of the Ando magmatic rock.

Sample	Rock type	Rb	Sr	$^{87}Rb/^{86}Sr$	$^{87}Sr/^{86}Sr$	±2σ	$(^{87}Sr/^{86}Sr)_i$	Sm	Nd	$^{147}Sm/^{144}Nd$	$^{143}Nd/^{144}Nd$	±2σ	$(^{143}Nd/^{144}Nd)_i$	ε$_{Nd}$(t)	T$^2_{DM}$ (Ga)	f$_{Sm/Nd}$
L13 AD51	Gabbro	17.6	107	0.4748	0.706191	0.000006	0.7050	3.13	9.28	0.2041	0.512926	0.000005	0.512690	5.5	0.51	-0.04
L13 AD53	Gabbro	42.7	101	1.2195	0.709980	0.000007	0.7069	2.68	8.16	0.1989	0.512865	0.000004	0.512635	4.4	0.60	-0.01
L13 AD33	high-Mg diorite	323	187	5.0131	0.734342	0.000007	0.7220	15.7	71.2	0.1339	0.512012	0.000005	0.511860	-10.8	1.83	-0.32
L13 AD34	high-Mg diorite	211	178	3.4334	0.729908	0.000006	0.7214	11.9	72.5	0.0990	0.511987	0.000004	0.511875	-10.5	1.82	-0.50
L13 AD02	calc-alkaline diorite	89.4	300	0.8622	0.719963	0.000005	0.7178	7.65	35.6	0.1302	0.512175	0.000005	0.512026	-7.5	1.57	-0.34
L13 AD04	calc-alkaline diorite	102	283	1.0451	0.719146	0.000005	0.7165	5.52	25.0	0.1337	0.512193	0.000004	0.512040	-7.3	1.55	-0.32
L13 AD45	Granodiorite	208	227	2.6557	0.737253	0.000006	0.7306	9.36	47.8	0.1187	0.512007	0.000004	0.511869	-10.6	1.82	-0.40
L13 AD47	Granodiorite	306	225	3.9383	0.740187	0.000007	0.7303	11.1	58.5	0.1150	0.511991	0.000005	0.511858	-10.8	1.84	-0.42

$^{87}Sr/^{86}Sr_{(i)} = (^{87}Sr/^{86}Sr)_{Sample} - (^{87}Rb/^{86}Sr)_{Sample} * (e^{\lambda T} - 1)$.
$\lambda_{Rb-Sr} = 0.0142$ Ga^{-1}; $\lambda_{Sm-Nd} = 0.00654$ Ga^{-1}.
$\varepsilon_{Nd}(t) = [(^{143}Nd/^{144}Nd)_{Sample}(T)/(^{143}Nd/^{144}Nd)_{CHUR}(T) - 1] * 10^4$.
$(^{143}Nd/^{144}Nd)_{Sample}(t) = (^{143}Nd/^{144}Nd)_{Sample} - (^{147}Sm/^{144}Nd)_{Sample} * (e^{\lambda T} - 1)$.
$(^{143}Nd/^{144}Nd)_{CHUR}(t) = 0.512638 - 0.1967 * (e^{\lambda T} - 1)$.
$T^2_{DM} = 1/\lambda * ln\{1 + [((^{143}Nd/^{144}Nd)_{Sample} - [(^{147}Sm/^{144}Nd)_{Sample} - 0.118] * (e^{\lambda T} - 1) - 0.513151)/(0.118 - 0.2136)]\}$.
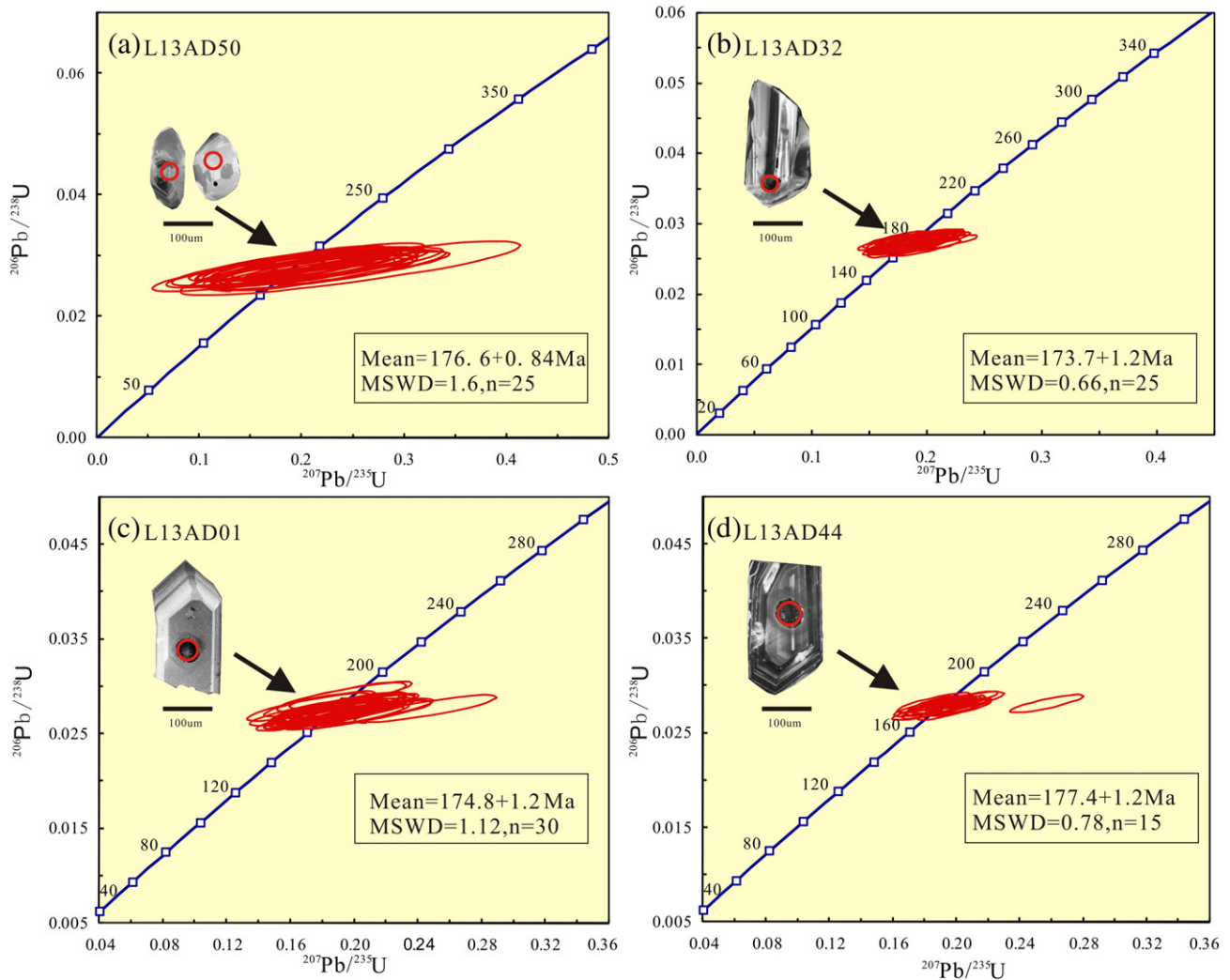
Fig. 3. Zircon U–Pb concordia diagrams of the Ando intrusive rocks in Southern Qiangtang terrane.

fields in the TAS diagram. They exhibit high-K characteristics in the SiO_2 versus K_2O diagram. These rocks display relatively steep REE patterns $((La/Yb)_N = 3.42–6.75; (Gd/Yb)_N = 1.68–1.83)$ with negative Eu anomalies $(\delta Eu = 0.55–0.73)$ (Fig. 5e). They are metaluminous (Fig. 4c) and show remarkable enrichments in LILE (such as Rb, K and Pb) and depletions in HFSE, with negative Nb-Ta-Ti anomalies, similar to subduction-related magmas (Fig. 5f).

The calc-alkaline granodiorites have high SiO_2 (62.16–65.99 wt.%), Al_2O_3 (15.77–18.15 wt.%), K_2O (2.67–4.98 wt.%) and Na_2O (2.48–3.56 wt.%) contents. The rocks show high-K affinities and plotted in the granodiorite field in the TAS plot (Fig. 4a and b). Their ASI index varies from 1.18 to 1.23, displaying a peraluminous character (Fig. 4c). The granodiorites samples also contain relatively low $Fe_2O_3^T$ (4.60–6.34 wt.%), MgO (1.81–2.46 wt.%), TiO_2 (0.63–0.85 ppm), and $Mg^\#$ (46–47). They are significantly enriched in LREEs and display slightly depleted HREEs $((La/Yb)_N = 11.28–29.86, (Ga/Yb)_N = 1.72–4.00)$, mostly with weak negative Eu anomalies (0.48–1.34) (Fig. 5g). These samples show pronounced negative Nb, Ta, Ti and Ba anomalies and positive K, Rb, Sr, Pb spikes in the primitive mantle-normalized trace element distribution patterns (Fig. 5h).

4.3. Sr–Nd isotope data

The Sr–Nd isotopic data of the studied rocks are presented in Table 2. The MORB-type gabbros show depleted Sr-Nd isotopic compositions, with positive $\varepsilon_{Nd}(t)$ ranging from 4.4 to 5.5 and initial $^{87}Sr/^{86}Sr$ ratios

from 0.7050 to 0.7069 (Fig. 6). The high-Mg diorites are characterized by enriched Sr-Nd isotopic compositions and have negative $\varepsilon_{Nd}(t)$ (−10.50 to −10.80) and high initial $^{87}Sr/^{86}Sr$ ratios (0.7214 to 0.7220), with old Nd model ages (T_{DM} = 1.82–1.83 Ga). The calc-alkaline diorites and granodiorites also possess enriched Sr-Nd compositions. They have slightly different negative $\varepsilon_{Nd}(t)$ (−7.3 to −7.5 for the diorites and −10.6 to −10.8 for the granodiorites, respectively) and high initial $^{87}Sr/^{86}Sr$ ratios (0.7165–0.7178, 0.7303–0.7306, respectively), with respective Nd model ages at 1.55–1.57 Ga and 1.82–1.84 Ga.

5. Petrogenesis

Our collected samples are very fresh and have very low loss on ignition (LOI) (0.63–1.42), which suggest an insignificant alteration or metamorphism after these rocks formed. Therefore, mobile elements (e.g., LILE) and immobile elements (e.g., HFSE) corresponding to hydrothermal fluids are both used to constrain the petrogenesis of these magmatic rocks.

5.1. Gabbro

Significant crustal contamination would modify both major-trace elements and radiogenic isotope compositions of basaltic melts (Castillo et al., 1999; X.-C. Wang et al., 2016). Therefore, the relation between major versus trace elements and elements versus radiogenic
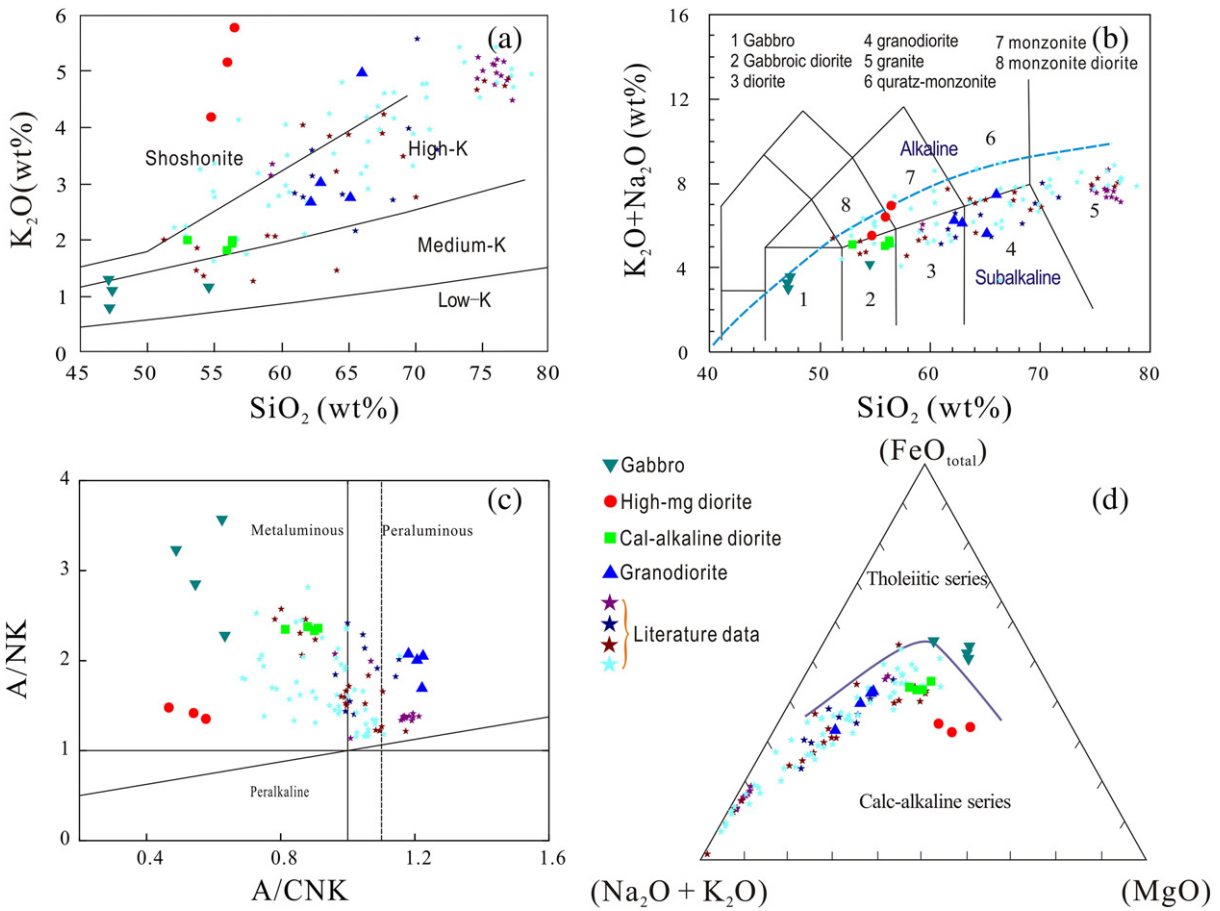
Fig. 4. Major element diagrams for the Ando Jurassic plutons. (a) alkaline and sub-alkaline division after Irvine and Baragar (1971); (b) TAS classification diagram (after Middlemost, 1994); (c) ANK versus ACNK diagram (after Maniar and Piccoli, 1989); (d) AFM diagram with boundary between the calc-alkaline and tholeiitic fields (after Irvine and Baragar, 1971), lava composition and trend lines for a typical sequence from Tingmuli volcano and a typical calc-alkaline trend from the Cascades lavas (after Carmichael, 1964). Literature data of Jurassic intrusive rocks are from Liu et al. (2014, 2015) and S.M. Li et al. (2014), J.X. Li et al. (2014).

isotopes can be used to evaluate the effect of crustal contamination on basaltic rocks (Wang et al., 2014). Although accumulation or crystallization of olivine, clinopyroxene, and plagioclase can modify both major and trace element contents, but ratios of highly incompatible trace elements remain untaken. Because crustal materials are characterized by low $\varepsilon Nd(t)$, Nb/La and Nb/Th and high $^{87}Sr/^{86}Sr$ ratios (Rudnick and Fountain, 1995), the high Nb/La and Nb/Th ratios of the Ando gabbros suggest an insignificant crustal contamination. Furthermore, the gabbros display a large range in Nb/La (0.88–3.54) and Nb/Th (7.43 to 15.60) ratios. If such various incompatible trace elements were caused by crustal input, the large range of initial Sr-Nd isotopes are also expected. However, the observed Sr-Nd isotopes of the gabbros have nearly constant values regardless their variations of the incompatible trace elements. This is inconsistent with the prediction of crustal contamination. Therefore, crustal contamination played an insignificant role in the formation of the Ando gabbros. This is also supported by the absence of old inherited zircons.

The Ando gabbros show relatively flat chondrite-normalized REE patterns ($(La/Yb)_N = 0.70–1.13$) and depleted $\varepsilon Nd(t)$ values (4.40–5.50), geochemically similar to MORB, indicating asthenosphere mantle was involved in the formation of the Ando gabbros. This is also supported by their similar Sr–Nd isotopic compositions to those of the Bangong-Nujiang ophiolites (Chen et al., 2015; B.D. Wang et al., 2016; K.J. Zhang et al., 2014; X.Z. Zhang et al., 2014). The gabbros have lower $(La/Sm)_{PM}$ ratios (0.70–0.93) than OIB (Sun and McDonough, 1989), and show relatively flat REE patterns with negative Nb-Ta anomalies. All of these features exclude a derivation from an OIB-like magma source. The weakly to strongly

negative Nb-Ta anomalies, various degrees of Th anomalies and strongly enriched in Pb are commonly related to crustal contamination (Rudnick and Gao, 2003) or fluid metasomatism in subduction zones (Donnelly et al., 2004). As demonstrated above, there are no remarkable crustal contamination in the formation of the Ando gabbros. The relatively flat REE patterns also exclude an origin from partial melting of an enriched mantle wedge formed by fluid metasomatism in subduction zones. Moreover, the occurrence of a large amount of aqueous minerals, such as hornblende, indicates that the gabbros were derived from a hydrous mantle source. Because asthenospheric mantle is hot and anhydrous, these hornblende minerals are not stable in convecting asthenosphere, but stable under the conditions of enriched lithospheric mantle (Class and Goldstein, 1997). This implies the lithospheric mantle has participated in the formation of the studied gabbros. Therefore, the gabbros were most likely derived from the upwelling asthenosphere-derived melts metasomatized by enriched lithospheric mantle.

Formation of enriched lithospheric mantle can be attributed to previous melts or fluids metasomatism in ancient subduction zones (Donnelly et al., 2004; Pearce et al., 2005). Generally, slab-derived fluids are enriched in LILE (e.g., K, Rb, Pb), depleted in HFSE (e.g., Nb, Ta, Ti), whereas LREE and Th are strongly partitioned into subducted oceanic slab-derived melts (Tatsumi and Eggins, 1995; Woodhead et al., 2001). The Ando gabbros are enriched in LILEs (e.g., K, Rb, Pb) and depleted in HFSEs (e.g., Nb and Ta). They have relatively high Ba/La (8–15), Ba/Th (29–150), U/Th (0.57–2.73) but low Th/Yb (0.05–0.33) and plot into the scope of slab-derived fluids on the Ba/La versus Th/Yb diagram (Fig. 7d). This suggests that the lithospheric metasomatism
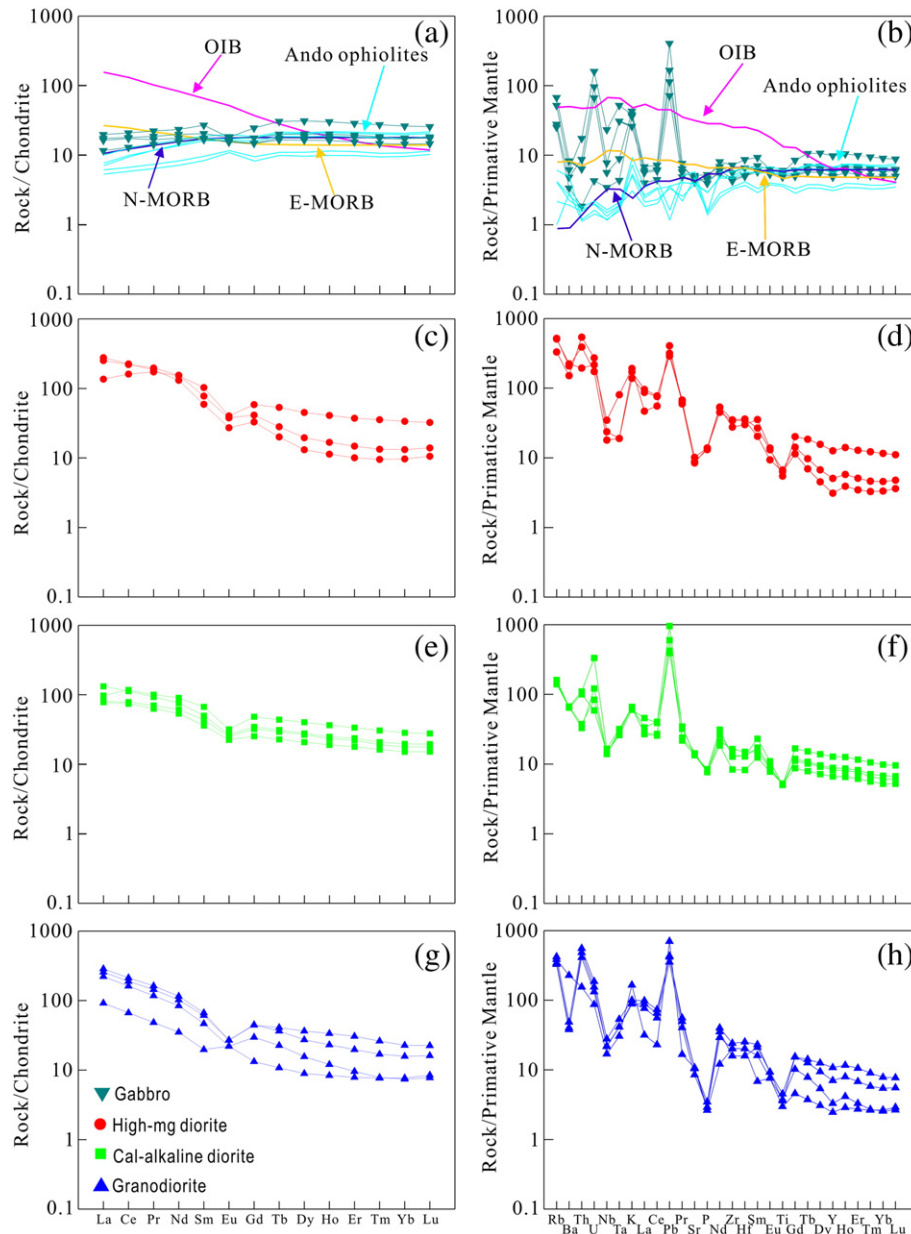
Fig. 5. Chondrite-normalized REE patterns and primitive mantle-normalized trace element variation diagrams for the Ando early-middle Jurassic plutons. (a–b) gabbro; (c–d) high-Mg diorite; (e–f) calc-alkaline diorite; (g–h) granodiorite. Normalizing values are from Sun and McDonough (1989). Ando ophiolite data are from B.D. Wang et al. (2016).

was deduced by ancient slab-derived aqueous fluids (Plank, 2005; Woodhead et al., 2001).

The gabbros possess variable Mg# (50–60) and compatible element concentrations (Ni = 39–144 ppm, Cr = 40–488 ppm), indicating the samples underwent various degrees of fractional crystallization. Their Mg# values are positively correlated with Ni and Cr contents (Fig. 7a and b), suggesting significant olivine and chromite fractional crystallizations. Moreover, the positive correlation between Mg# and CaO indicates clinopyroxene fractionation (Fig. 7c). Because of much higher SiO$_2$, sample L13 AD52 probably involved more significant fractional crystallization of mafic minerals. Therefore, The Ando gabbros were formed by interactions between the asthenospheric-derived melts and the overlying lithospheric mantle, then underwent fractional crystallization of mafic minerals during the magma rising.

The melting depths of the gabbros can be modeled using the related trace elements. Different minerals have different partition coefficient for trace elements. Garnet has high partition coefficient for Yb, whereas La, Sm are incompatible in garnet, which has almost the same partition for

La and Sm (Aldanmaz et al., 2000). Therefore, various degrees of partial melting of a garnet-lherzolite source region (with garnet residue) produce melts with significantly decreasing Yb and increasing Sm/Yb ratios than the mantle source. In consequence, the garnet-lherzolite melting trend is displaced from the mantle array to higher Sm/Yb ratios on an Sm/Yb against La/Sm diagram. However, spinel has almost unanimous partition coefficients for Sm and Yb, partly dissolving of the spinel lherzolite mantle can not change the Sm/Yb ratios. Melting of a spinel-lherzolite source will therefore create a approximately horizontal melting trend, which lies within or close to a mantle array defined by DMM and PM compositions (Aldanmaz et al., 2000; Jung et al., 2006). The Ando gabbros define a relatively horizontal line trend in a La/Sm versus Sm/Yb diagram (Fig. 8a), with increasing La/Sm ratios at nearly constant Sm/Yb ratios. The low and constant Sm/Yb ratios suggest that the gabbros were derived from partial melting of a spinel-facies lherzolite mantle, indicating a relatively shallow depth of melting (<80 km). This is also supported by the La/Yb versus Dy/Yb diagram (Fig. 8b), in which the Ando gabbros plot in the stability field of spinel peridotite.
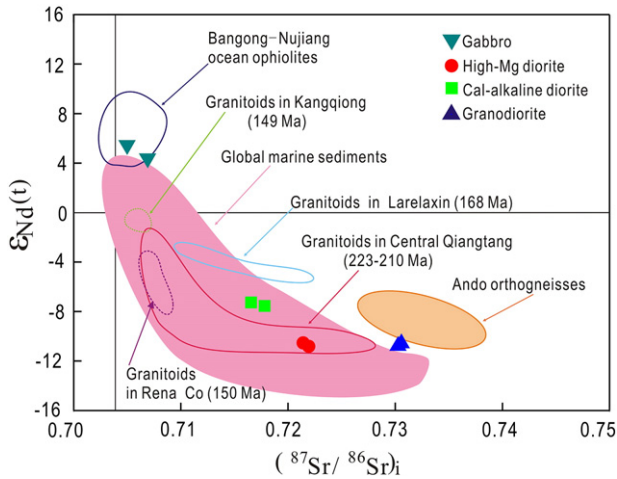
Fig. 6. $\varepsilon_{Nd}(t)$ versus $(^{87}Sr/^{86}Sr)_i$. Date sources are as follows: Ando orthogneiss from Harris et al. (1988), Global marine sediments from Plank and Langmuir (1998), Bangong-Nujiang Ocean ophiolites from K.J. Zhang et al. (2014) and X.Z. Zhang et al. (2014), Granitoids in Larelaxin from Liu et al. (2014), Granitoids in Central Qiangtang from Zhai et al. (2013) and Li et al. (2015), Granitoids in Rena Co from Hao et al. (2015) and Granitoids in Kangqiong from Li et al. (2015).

5.2. High-Mg diorite

The diorite samples have high MgO (8.30–10.24 wt.%) and $Mg^{\#}$ (70–74), and fall in the high-Mg andesite (HMA) field in the SiO_2 versus MgO diagram (Fig. 9a). The high-Mg diorites are generally divided into four petrogenesis groups: sanukitoid, boninite, bajaite and high-Mg adakite (Kamei et al., 2004; Smithies and Champion, 2000). Sanukitoid is characterized by strong LILE and LREE enrichments, low HREE contents, high Cr and Ni contents and high $Mg^{\#}$, relatively high Y (>10 ppm) and Yb (>0.8 ppm), low Sr/Y (<40) and $(La/Yb)_N$ (<10) ratios (Kamei et al., 2004; Martin et al., 2005). It is generated by reaction of a silicic melt derived from a subducting oceanic slab with a mantle peridotite (Kelemen et al., 2003; Tatsumi and

Hanyu, 2003; Wang et al., 2011). Boninite is characterized by high SiO_2 (> 52 wt.%), MgO (> 8 wt.%), very low TiO_2 (< 0.5 wt.%), depletion of HFSE and REE, and enrichment of LILE (Saunders et al., 1987). The rock is suggested to be produced by partial melting of depleted mantle source fluxed by slab-derived fluids (Crawford et al., 1989) or disequilibrium reaction of a mantle peridotite with a silicic melt derived from partial melting of a subducting oceanic slab (Saunders et al., 1987). Bajaite has very high Ba (>1000 ppm), Sr (Sr up to 4000 ppm), K/Rb (>1000) and Sr/Y (45–506), but low Rb/Sr (<0.01), depletion in HREE and HFSE (Rogers et al., 1985). It is considered to be produced by disequilibrium interaction between mantle peridotite and slab-derived Si-rich melts (Rogers et al., 1985). High-Mg adakite has high Sr (>400 ppm), Sr/Y and $(La/Yb)_N$ ratios, low Y (<18 ppm) and Yb (<1.9 ppm) (Defant and Drummond, 1990). It is usually derived from melting of subducted oceanic slab, which react with mantle wedge (Smithies and Champion, 2000) or thickened lower crust (Atherton and Petford, 1993).

The Ando high-Mg diorites have relatively high TiO_2 (>1%), excluding a petrogenesis of boninite. Their low Sr (178–215 ppm) contents make them different from bajaites. Their low Sr, Sr/Y and relatively high Y are also different from adakites. The high-Mg diorites are characterized by enrichment of LILE and LREE, high $Mg^{\#}$(70–74), Cr (400–547 ppm) and Ni (120–152 ppm) contents, low HREE, Sr/Y and La/Yb ratios (Table 1), significant negative anomalies of Nb and Ti and positive anomaly of Pb, which are quite analogous to those of Cenozoic sanukites in the Setouchi Volcanic Belt (Martin et al., 2005; Tiepolo and Tribuzio, 2008). This indicates a close affinity of sanukites for the high-Mg diorites, which is also supported by plots of MgO (wt.%) vs. SiO_2, Sr/Y versus Y. (Fig. 9a and b). Therefore, the high-Mg diorites have similar petrogenesis to typical sanukites generated by reaction of subducting slab and/or sediment-derived melts with a mantle wedge.

Except for the above possible petrogenesis, there are three potential models to interpret the formation of the high-Mg diorites, including; (1) mafic magma with crustal contamination, (2) fractional crystallization (FC) from parental basic magmas, (3) mixing between felsic and basaltic magmas (Streck et al., 2007). The first two models are not applicable to the Ando high-Mg diorites, because the coeval mafic magmas in this area (e.g., the MORB-type gabbros) have lower MgO, Cr, Ni than the
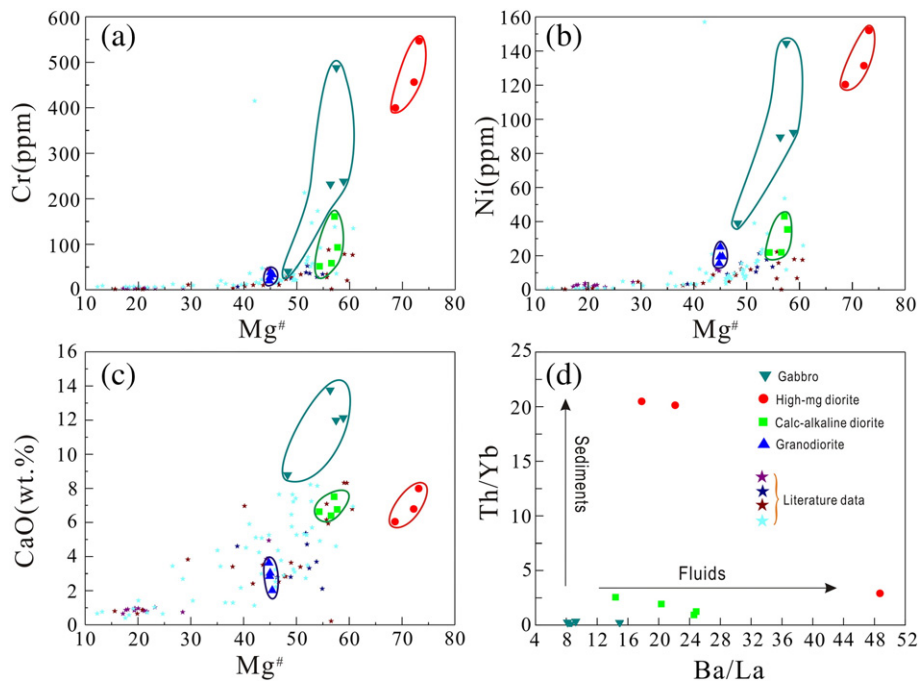

Fig. 7. (a) $Mg^{\#}$ vs Cr, (b) $Mg^{\#}$ vs Ni and (c) $Mg^{\#}$ vs CaO diagrams for the Ando Jurassic magmatic rocks. (d) Ba/La vs Th/Yb diagram for the Ando gabbros, high-Mg diorite, calc-alkaline diorite after (Woodhead et al., 2001). Literature data of Jurassic intrusive rocks are same to Fig. 4.
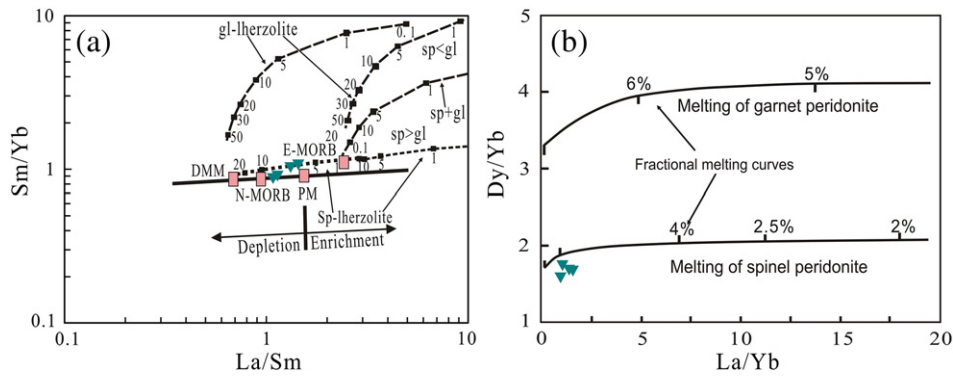
Fig. 8. (a) La/Sm vs Sm/Yb (after Aldanmaz et al., 2000) and (b) La/Yb versus Dy/Yb diagrams for the Ando gabbros (after Jung et al., 2006).

high-Mg diorites. If the mafic magmas undergone contamination of continental crust or fractional crystallization, their MgO, Cr, Ni contents will decrease obviously. The mixing model is also inconsistent with the high-Mg diorites, because their very high Mg# and low $\varepsilon_{Nd}(t)$ values (-10.80 to -10.50) do not support a significant input of crustal felsic magmas.

The high-Mg diorites exhibit low $\varepsilon_{Nd}(t)$ (-10.80 to -10.50) values, high K_2O ($K_2O/Na_2O = 3.19$–5.04) and Ba (> 1000 ppm). Because K is enriched in clay minerals of deep-sea muds and shales, whereas Ba is dominated in plagioclase of turbidites, the high K and Ba characters of the high-Mg diorites are most likely produced by partial melting of subducted marine sediments (Plank and Langmuir, 1998). In addition, sediment-derived melts could notably enhance La/Sm ratios of the magma (Fig. 9c), but it could not change Ba/Th ratios (Tatsumi, 2006). The high-Mg diorites have relatively high La/Sm, low Ba/Th. As shown in Th/Yb versus Sr/Nd, the high-Mg diorites plot parallel to the Th/Yb axis (Fig. 9d), demonstrating that the mantle source of the diorites was metasomatized by subducted oceanic sediment-derived melts (Woodhead et al., 1998). All these evidence suggest that the high-Mg

diorites were probably generated by the interaction of subducted oceanic sediment-derived melts and mantle peridotites. Hydrous minerals (hornblende) exist in the high-Mg diorites, which suggests that primitive parental melts are hydrous. This is supported by their relatively high Ba/La ratios, because Ba is more soluble in aqueous fluids than La (Hanyu et al., 2006). Therefore, we infer that not only sediment-derived melts but also slab-derived aqueous fluids have been involved in the magma generation.

5.3. Calc-alkaline diorite

Comparing with the high-Mg diorites, the diorites have relatively low MgO, Mg#, Cr, Ni, and high FeO^T values (Table 1), showing calc-alkaline characters in the AFM diagram (Fig. 4d). Although the rocks still fall in the HMA field in the SiO_2 versus MgO diagram (Fig. 9a), it is impossible for them to be derived from the high-Mg diorite magma with significant fractional crystallization due to their relatively low SiO_2, high MgO, Mg#, Cr, Ni and moderate TiO_2 and $Fe_2O_3^T$ contents. In addition, the Ando calc-alkaline diorites have higher $\varepsilon_{Nd}(t)$ values
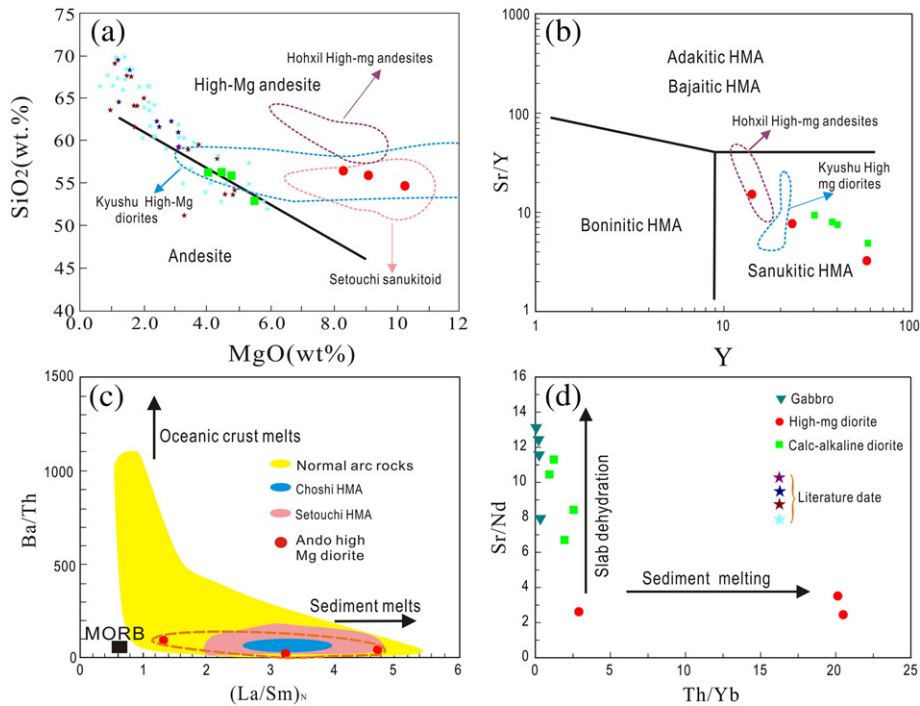

Fig. 9. (a) MgO vs. SiO_2 correlation diagram for distinguishing high-Mg andesite from normal andesite (after McCarron and Smellie, 1998). Sanukitoid data of Setouchi volcanic belt are from Tatsumi and Hanyu (2003) and magnesian andesite data of Baja California are from Calmus et al. (2003). (b) Sr/Y vs. Y distinguishing diagram for the Ando high-Mg diorites (after Kamei et al., 2004). (c) Ba/Th vs. (La/Sm)$_N$ distinguishing diagrams for the Ando high-Mg diorites. Data of Choshi and Setouchi high-Mg andesites and normal arc rocks are from Tatsumi (2006) and Hanyu et al. (2006). (d) Sr/Nd vs Th/Yb distinguishing diagram (after Woodhead et al., 1998) for the Ando Jurassic plutons. Literature data of Jurassic intrusive rocks are same to Fig. 4.

than the high-Mg diorites, further excluding fractional crystallization from the high-Mg diorites magma. In subduction zone, mafic to intermediate magmas are generally produced by partial melting of mantle wedge peridotites (Hildreth and Moorbath, 1988). The negative $\varepsilon_{Nd}(t)$ values (-7.5 to -7.3), however, suggest that the calc-alkaline diorites cannot be derived from a mantle wedge directly. Because their $\varepsilon_{Nd}(t)$ values are similar to those of Ando basement rocks (Fig. 6), it is likely that the calc-alkaline diorites were derived from the crustal anatexis with/without significant input of mantle components. The old Nd crustal model ages (1.82–1.83 Ga) suggest that the basement rocks of the Ando microcontinent are possible source material for the calc-alkaline diorites. Mafic lower crust-derived melts are characterized by low $Mg^{\#}$ (<40) regardless of melting degrees, whereas those with $Mg^{\#} > 40$ can only be obtained with involvement of a mantle component (Patiño Douce, 1999; Rapp and Watson, 1995). Their relatively high $Mg^{\#}$ and $\varepsilon_{Nd}(t)$ values, however, indicate an input of mantle components. These features, therefore, suggest that the diorites were most likely produced by partial melting of the Ando basement rocks with significant input of mantle components.

5.4. Calc-alkaline granodiorite

The granodiorites have enrichments in Rb, K, U, Th, Pb and depletions in HFSEs, with pronounced negative Nb-Ta-Ti anomaly and negative Eu anomalies, similar to continental crust (Rudnick and Fountain, 1995). The rocks are peraluminous (ASI > 1.1) (Fig. 4c) and their relatively high SiO_2 and low P_2O_5 make up a linear relationship (no showing), showing typical features of I-type granites (Chappell and White, 2001). Their $\varepsilon_{Nd}(t)$ and initial $^{87}Sr/^{86}Sr$ isotopic ratios are close to the Ando basement ($\varepsilon_{Nd}(t) = -7.49$ to -9.56, $(^{86}Sr/^{87}Sr)_i = 0.7268–0.7383$, Harris et al., 1988). This indicates that the granodiorites were possibly derived from partial melting of the basement rocks (Fig. 6). These geochemical characteristics further suggest a derivation from partial melts of granitic gneisses in the basement. This interpretation is also supported by the old inherited zircons from our samples. Therefore, we suggest that the granodiorites were generated by partial melting of the Ando basement.

6. Discussion

6.1. Tectonic setting in the Mesozoic

The Mesozoic is a critical period for the magmatic and tectonic evolution in the Southern Qiangtang terrane. Mesozoic plutons from the southern Qiangtang terrane are poorly known due to the limited outcrops in early studies (Guynn et al., 2006; Kapp et al., 2005). Recently, lots of Jurassic intermediate-felsic intrusions, including coeval calc-alkaline, highly fractionated I-type granites with mafic enclaves, alkaline and peralkaline granitoids, have been newly discovered along the southern margin of the Southern Qiangtang terrane (S.M. Li et al., 2014; J.X. Li et al., 2014; Liu et al., 2014, 2015; Pullen et al., 2011). Based on geochemical studies, these Jurassic magmatic rocks were interpreted to be the products of the northward subduction of the Bangong–Nujiang Ocean (Kapp et al., 2005; Liu et al., 2011; Pullen et al., 2011). Although these intrusive rocks was suggested to be formed due to the northward subduction of the Bangong–Nujiang Ocean, the initial subduction time of this ocean is still unclear. Zhu et al. (2013) suggested the Bangong–Nujiang ocean began northward subduction beneath the Southern Qiangtang terrane as early as the middle-late Triassic. Recently, abundant late Triassic (~210 Ma) arc-related magmatic rocks are also exposed in the Central Qiangtang (Fu et al., 2010; Peng et al., 2015; X.Z. Zhang et al., 2014), which represent the early-stage of a magmatic arc induced by the northward subduction of the Bangong–Nujiang Ocean (Zeng et al., 2015). Based on the research of sedimentary rocks and associated magmatic rocks in Southern-Central Qiangtang, the northward subduction of the Bangong–Nujiang

ocean was suggested to start even before middle-late Triassic (Chen et al., 2015, 2016; Zeng et al., 2015). However, structural and sedimentological studies argued that the subduction of this ocean most likely initialed earlier in the east near Ando, but later in the west near Bangong Co (Yin and Harrison, 2000).

In the Ando area, Mesozoic granites were mainly formed in the Jurassic (Liu, 2012). Because the granites are enriched in alkali, they were considered to be generated in a post-collision setting (Liu et al., 2011; Liu, 2012). In this study, however, the Jurassic MORB-type gabbros, high-Mg diorites, calc-alkaline diorites and granodiorites entirely show arc affinity, providing reliable evidence for the existence of a Mesozoic continental arc once built on the Ando terrane. Based on the research of basement rocks and ophiolites in this area, the Ando terrane was suggested to be an isolated microcontinent during the Permian–Triassic and subjected to northward subduction in the Early Jurassic, resulting in metamorphism up to HP granulite-facies (Coward et al., 1988; Guynn et al., 2006, 2012; Shi et al., 2012; Xu et al., 1985; Zhang et al., 2012; K.J. Zhang et al., 2014; Zhu et al., 2013). Zircon U–Pb dating of our studied samples indicates that the various Ando intrusive rocks formed during the time between 173.7 Ma and 177.4 Ma. The intrusive ages of these arc-related plutons, therefore, suggest that the beginning of northward subduction of the Bangong–Nujiang Ocean is prior to the middle Jurassic.

Recently, voluminous slightly younger granitoids (170–150 Ma) were continuously discovered along the southern margin of the Southern Qiangtang, not limitedly outcropped in the Ando microcontinent (Kapp et al., 2005; S.M. Li et al., 2014; Liu et al., 2014, 2015; Pullen et al., 2011). Based on geochronological and geochemical studies of these granitoids, Guynn et al. (2006) suggested that a Jurassic arc developed along the southern Qiangtang terrane during the northward subduction of the Bangong–Nujiang ocean. This tectonic setting is also supported by some recent achievements, e.g., the Jurassic arc-related magmatic rocks exposed from Bangong Tso, though Gaize, to Ando (S.M. Li et al., 2014; Liu et al., 2015). All these Jurassic rocks show typical arc geochemical character and thus were considered as results of a Mesozoic magmatic arc (Kapp et al., 2005; J.X. Li et al., 2014; Liu et al., 2014). The above lines of evidence, therefore, indicate a tectonic setting of continent arc deduced by a northward subduction of the Bangong–Nujiang ocean underneath the Southern Qiangtang terrane during the early Mesozoic.

6.2. Geodynamics model

Although the published date suggest that the Bangong–Nujiang ocean was sudducted northward beneath the Southern Qiangtang terrane during the Jurassic (Liu et al., 2011; Liu, 2012; S.M. Li et al., 2014; J.X. Li et al., 2014), the petrogenesis of the Ando MORB-type gabbros and high-Mg diorites could not be explained by a normal oceanic slab subduction. These special rock types were generally generated under abnormal high temperature that was related to a slab roll-back environment, ridge subduction environment or slab break-off environment. In these environments, the upwelling of asthenosphere will heat the subducting slab (Ayabe et al., 2012; Sato et al., 2014) or subcontinental lithosphere mantle to form the MORB-type gabbros and high-Mg diorites (Coney and Reynolds, 1977; McKenzie and Bickle, 1988). The Zr saturation temperatures indicate that the Ando granodiorites were generated at high temperatures (793–836 °C). Additionally, estimated by plagioclase and hornblende, the Jurassic granitoids were suggested to be high-temperature and low-pressure types, also indicating a possible asthenospheric upwelling (Liu, 2012). Liu (2012) suggested that the Ando early-middle Jurassic magmatism was triggered by a slab break-off due to the collision between the Ando microcontinent and the South Qiangtang terrane. However, there are no coeval high-temperature magmatic rocks exposed in the Qiangtang terrane to the north of the Ando microcontinent, ruling out a slab break-off setting. Because 185–150 Ma magmatism occurs in a linear distribution along the

southern margin of the Qiangtang terrane, it is impossible for our studied rocks formed in a ridge subduction environment.

Because the formation of the different Jurassic magmatic rocks needs abnormal high temperatures, we suggest that a slab roll-back probably played a key role in the generation of these rocks. The slab roll-back model can well explain the linear distribution of the Jurassic magmatic rocks (Kapp et al., 2005; Liu et al., 2011; Liu, 2012; J.X. Li et al., 2014; Liu et al., 2015). During late Triassic to early Jurrassic, the Bangong–Nujiang Ocean lithosphere subducted northward at a low angle beneath the Qiangtang terrane, which result the widely distributed abundant late Triassic (~210 Ma) magmatic rocks in the Central Qiangtang (Zeng et al., 2015). In the Jurassic, the magmatic front moved further south due to the normal angle subduction. Then, a magmatic gap in the Southern Qiangtang from middle-late Trassic to early Jurassic indicates the beginning of a "flat-subduction". The Jurassic high-temperature magmas along the Southern Qiangtang mark the appearance of slab roll-back. In southern Qiangtang, a younger age trend of magmatic rocks from north to south is consistent with the a slab roll-back model. This model is also supported by Some Jurassic magmatic rocks and their mafic–intermediate enclaves in the south Qiangtang terrane. The magmatic rocks have relatively high compatible elements (Fig. 7a-c) and wide ranges of Sr-Nd isotopes, suggesting a significant input of mantle-derived components (S.M. Li et al., 2014; J.X. Li et al., 2014; Liu et al., 2014). The occurrence of mafic–intermediate enclaves corroborate the mantle component underplated beneath the Qiangtang terrane (S.M. Li et al., 2014; J.X. Li et al., 2014; Liu et al., 2015).

Slab roll-back was associated with the northward subduction of the Bangong–Nujiang Ocean lithosphere, therefore, has been proposed to explain the generation of the MORB-type gabbros, high-Mg diorites, calc-alkaline diorites and granodiorites exposed in the Ando area, center Tibet (Fig. 10). The subducting slab migrates backwards to the asthenospheric mantle (roll-back) and therefore results in the hot asthenospheric mantle upwelling and decompression melting. The asthenosphere-derived melts reacted with the overlying enriched lithospheric mantle metasomatized by ancient slab-derived aqueous fluids, forming the MORB-type tholeiitic gabbros. The asthenospheric upwelling results in high temperature conditions that led to the relative cold subducted slab was effectively reheated to cause sediment melting. These sediment-derived melts reacted with the mantle wedge and then partial melting of the metasomatized mantle peridotites generated the high-Mg diorites. Triggered by the upwelling asthenosphere, the calc-alkaline diorites and granitoids were produced by partial melting

of the lower crust (Ando basement) with/without significant input of mantle components, respectively.

7. Conclusions

(1) The gabbros, high-Mg diorites, calc-alkaline diorites and granodiorites exposed in the Ando area were synchronously emplaced at 174–177 Ma.

(2) The MORB-type gabbros were generated by the reaction of upwelling asthenosphere-derived melts with sub-continental lithospheric mantle metasomatized by ancient slab-derived aqueous fluids. The high-Mg diorites were most likely produced by partial melting of metasomatized mantle peridotites.

(3) The high-K calc-alkaline diorites and granodioritse were formed by partial melting of the Ando basement rocks with and without significant input of mantle components, respectively.

(4) The formations of these Jurassic intrusive rocks were triggered by the asthenospheric upwelling that was resulted from the slab roll-back of the subducted Bangong–Nujiang Ocean.

Supplementary data to this article can be found online at http://dx.doi.org/10.1016/j.lithos.2016.09.002.

References

Abratis, M., Worner, G., 2001. Ridge collision, slab-window formation, and the flux of Pacific asthenosphere into the Caribbean realm. Geology 29, 127–130.

Aldanmaz, E., Pearce, J.A., Thirlwall, M.F., Mitchell, J.G., 2000. Petrogenetic evolution of late Cenozoic, post-collision volcanism in western Anatolia, Turkey. Journal of Volcanology and Geothermal Research 102, 67–95.

Andersen, T., 2002. Correction of common lead in U –Pb analyses that do not report ^{204}Pb. Chemical Geology 192, 59–79.
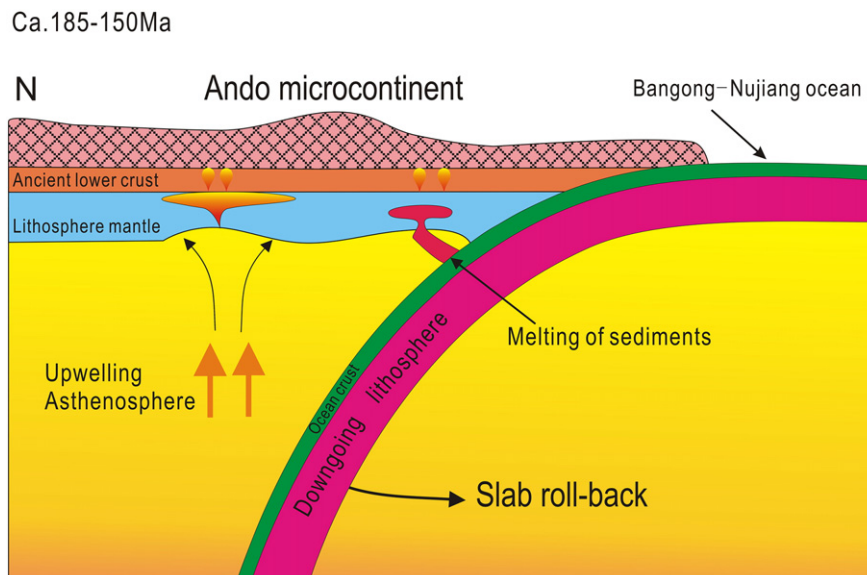
Ca.185-150Ma

Fig. 10. A slab roll-back model for the generation of the Ando Jurassic plutons.

Atherton, M.P., Petford, N., 1993. Generation of sodium-rich magmas from newly underplated basic crust. Nature 362, 144–146.

Ayabe, M., Takanashi, K., Shuto, K., Ishimoto, H., Kawabata, H., 2012. Petrology and geochemistry of adakitic dacite and high-MgO andesites, and related calc-alkaline dacites from the Miocene Okoppe volcanic field, Northeast Hokkaido, Japan. Journal of Petrology 53, 547–588.

Bureau of Geology of Tibet Autonomous Region (BGTAR), 2005. The special report of regional geological survey of the People's Republic of China: composition and tectonic evolution of Nierong complex in northern Tibet (1:250000)–Naqu town. pp. 1–43 (in Chinese).

Calmus, T., et al., 2003. Spatial and temporal evolution of basalts and magnesian andesites ("bajaites") from Baja California, Mexico: the role of slab melts. Lithos 66, 77–105.

Carmichael, I.S.E., 1964. The petrology of Thingmuli, a Tertiary volcano in Eastern Iceland. Journal of Petrology 5, 435–460.

Castillo, P.R., Janney, P.E., Solidum, R.U., 1999. Petrology and geochemistry of Camiguin island, southern Philippines: insights to the source of adakites and other lavas in a complex arc setting. Contributions to Mineralogy and Petrology 134, 33–51.

Chappell, B.W., White, A.J.R., 2001. Two contrasting granite types: 25 years later. Australian Journal of Earth Sciences 48, 489–499.

Chen, B., Arakawa, Y., 2005. Nd–Sr isotopic geochemistry of granitoids from the West Junggar fold belt (NW China), with implications for Phanerozoic continental growth. Geochimica et Cosmochimica Acta 69, 1307–1320.

Chen, J.L., Xu, J.F., Wang, B.D., Kang, Z.Q., Li, J., 2010. Origin of Cenozoic alkaline potassic volcanic rocks at Konglongxiang, Lhasa terrane, Tibetan Plateau: Products of partial melting of a mafic lower-crustal source? Chemical Geology 273, 286–299.

Chen, S.S., Shi, R.D., Zou, H.B., Huang, Q.S., Liu, D.L., Gong, X.H., Yi, G.D., Wu, K., 2015. Late Triassic island-arc–back-arc basin development along the Bangong–Nujiang suture zone (central Tibet): geological, geochemical and chronological evidence from volcanic rocks. Lithos 230, 30–45.

Chen, S.S., Shi, R.D., Yi, G.D., Zou, H.B., 2016. Middle Triassic volcanic rocks in the Northern Qiangtang (Central Tibet): geochronology, petrogenesis, and tectonic implications. Tectonophysics 666, 90–102.

Chung, S.L., Chu, M.F., Zhang, Y.Q., Xie, Y.W., Lo, C.H., Lee, T.Y., Lan, C.Y., Li, X.H., Zhang, Q., Wang, Y.Z., 2005. Tibetan tectonic evolution inferred from spatial and temporal variations in post-collisional magmatism. Earth-Science Reviews 68, 173–196.

Class, C., Goldstein, S.L., 1997. Plume–lithosphere interactions in the ocean basins: constrains from the source mineralogy. Earth and Planetary Science Letters 150, 245–260.

Coney, P.J., Reynolds, S.J., 1977. Cordilleran Benioff zones. Nature 270, 403–406.

Corfu, F., Hanchar, J.M., Hoskin, P.W.O., Kinny, P., 2003. Atlas of zircon textures. Reviews in Mineralogy and Geochemistry 53, 469–500.

Coward, M.P., Kidd, W.S.F., Yun, P., et al., 1988. The structure of the 1985 Tibet Geotraverse, Lhasa to Golmud. Philosophical Transactions of the Royal Society of London, Series A: Mathematical, Physical and Engineering Sciences 327, 307–336.

Crawford, A.J., Falloon, T.J., Green, D.H., 1989. Classification Petrogenesis and Tectonic Setting of Boninites. In: Crawford, A.J. (Ed.), Boninites. Academic Division of Unwin Hyaman, Ltd., London, pp. 1–49.

Davies, J.H., von Blanckenburg, F., 1995. Slab breakoff: a model of lithosphere detachment and its test in the magmatism and deformation of collisional orogens. Earth and Planetary Science Letters 129, 85–102.

DeCelles, P.G., Robinson, D.M., Zandt, G., 2002. Implications of shortening in the Himalayan fold-thrust belt for uplift of the Tibetan Plateau. Tectonics 21, 1062. http://dx.doi.org/10.1029/2001TC001322.

Defant, M.J., Drummond, M.S., 1990. Derivation of some modern arc magmas by melting of young subduction lithosphere. Nature 347, 662–665.

Ding, L., Kapp, P., Wan, X., 2005. Paleocene–Eocene record of ophiolite obduction and initial India–Asia collision, south central Tibet. Tectonics 24, 1–18.

Ding, L., Kapp, P., Yue, Y., Lai, Q., 2007. Postcollisional calc-alkaline lavas and xenoliths from the southern Qiangtang terrane, central Tibet. Earth and Planetary Science Letters 254, 28–38.

Donnelly, K.E., Goldstein, S.L., Langmuir, C.H., Spiegelman, M., 2004. Origin of enriched ocean ridge basalts and implications for mantle dynamics. Earth and Planetary Science Letters 226, 347–366.

Fu, X.G., Wang, J., Tan, F.W., Chen, M., Chen, W.B., 2010. The Late Triassic rift-related volcanic rocks from eastern Qiangtang, northern Tibet (China): age and tectonic implications. Gondwana Research 17, 135–144.

Guivel, C., Lagabrielle, Y., Bourgois, J., Maury, R.C., Fourcade, S., Martin, H., Arnaud, N., 1999. New geochemical constraints for the origin of ridge subduction-related plutonic and volcanic suites from the Chile Triple Junction (Taitao Peninsula and Site 862, LEG ODP141 on the Taitao Ridge). Tectonophysics 311, 83–111.

Guivel, C., Morata, D., Pelleter, E., Espinoza, F., Maury, R.C., Lagabrielle, Y., Polvé, M., Bellon, H., Cotten, J., Benoit, M., Suárez, M., de la Cruz, R., 2006. Miocene to Late Quaternary Patagonian basalts (46–47°S): geochronometric and geochemical evidence for slab tearing due to active spreading ridge subduction. Journal of Volcanology and Geothermal Research 149, 346–370.

Guynn, J.H., Kapp, P., Pullen, A., Heizler, M., Gehrels, G., Ding, L., 2006. Tibetan basement rocks near Ando reveal "missing" Mesozoic tectonism along the Bangong suture, central Tibet. Geology 34, 505–508.

Guynn, J., Kapp, P., Gehrels, G.E., Ding, L., 2012. U–Pb geochronology of basement rocks in central Tibet and paleogeographic implications. Journal of Asian Earth Sciences 43, 23–50.

Hanyu, T., Tatsumi, Y., Nakai, S.I., Chang, Q., Miyazaki, T., Sato, K., Tani, K., Shibata, T., Yoshida, T., 2006. Contribution of slab melting and slab dehydration to magmatism in the NE Japan arc for the last 25 Myr: constraints from geochemistry. Geochemistry, Geophysics, Geosystems 7, 1–29.

Hao, L.L., Wang, Q., Wyman, D.A., Ou, Q., Dan, W., Jiang, Z.Q., Wu, F.Y., Yang, J.H., Long, X.P., Li, J., 2015. Underplating of basaltic magmas and crustal growth in a continental arc: Evidence from Late Mesozoic intermediate–felsic intrusive rocks in southern Qiangtang, central Tibet. Lithos 245, 223–242.

Harris, N.B.W., Holland, T.J.B., Tindle, A.G., 1988. Metamorphic rocks of the 1985 Tibet Geotraverse, Lhasa to Golmud. Philosophical Transactions of the Royal Society of London, Series A: Mathematical, Physical and Engineering Sciences 327, 203–213.

Hildreth, W., Moorbath, S., 1988. Crustal contributions to arc magmatism in the andes of Central Chile. Contributions to Mineralogy and Petrology 98, 455–489.

Irvine, T.N., Baragar, W.R.A., 1971. A guide to the chemical classification of the common volcanic rocks. Canadian Journal of Earth Sciences 8, 523–548.

Jahn, B.M., Capdevila, R., Liu, D., Vernon, A., Badarch, G., 2004. Sources of Phanerozoic granitoids in the transect Bayanhongor-Ulaan Baatar, Mongolia: geochemical and Nd isotopic evidence, and implications for Phanerozoic crustal growth. Journal of Asian Earth Sciences 23, 629–653.

Jung, C., Jung, S., Hoffer, E., Berndt, J., 2006. Petrogenesis of Tertiary mafic alkaline magmas in the Hocheifel, Germany. Journal of Petrology 47, 1637–1671.

Kamei, A., Owada, M., Nagao, T., Shiraki, K., 2004. High-Mg diorites derived from sanukitic HMA magmas, Kyushu Island, southwest Japan arc: evidence from clinopyroxene and whole rock compositions. Lithos 75, 359–371.

Kapp, P., Yin, A., Manning, C.E., Murphy, M., Harrison, T.M., Spurlin, M., Lin, D., Deng, X.G., Wu, C.M., 2000. Blueschist-bearing metamorphic core complexes in the Qiangtang block reveal deep crustal structure of northern Tibet. Geology 28, 19–22.

Kapp, P., Yin, A., Manning, C.E., Harrison, T.M., Taylor, M.H., Ding, L., 2003. Tectonic evolution of the early Mesozoic blueschist-bearing Qiangtang metamorphic belt, central Tibet. Tectonics 22, 1043 (1010.1029/2002TC001386).

Kapp, P., Yin, A., Harrison, T.M., Ding, L., 2005. Cretaceous–Tertiary shortening, basin development, and volcanism in central Tibet. Geological Society of America Bulletin 117, 865–878.

Kapp, P., DeCelles, P.G., Gehrels, G.E., Heizler, M., Ding, L., 2007. Geological records of the Lhasa–Qiangtang and Indo-Asian collisions in the Nima area of central Tibet. Geological Society of America Bulletin 119, 917–932.

Karsli, O., Dokuz, A., Uysal, I., Aydin, F., Chen, B., Kandemir, R., Wijbrans, J., 2010. Relative contributions of crust and mantle to generation of Campanian high-K calc-alkaline I-type granitoids in a subduction setting, with special reference to the Harsit Pluton, eastern Turkey. Contributions to Mineralogy and Petrology 160, 467–487.

Kay, S.M., Mpodozis, C., 2001. Central Andean ore deposits linked to evolving shallow subduction systems and thickening crust. GSA Today 11, 4–9.

Kelemen, P.B., Rilling, J.L., Parmentier, E.M., Mehl, L., Hacker, B.R., 2003. Thermal structure due to solid-state flow in the mantle wedge beneath arcs. Inside the Subduction Factory 138, pp. 293–311.

Li, X.H., Liu, D.Y., Sun, M., Li, W.X., Liang, X.R., Liu, Y., 2004. Precise Sm–Nd and U–Pb isotopic dating of the supergiant Shizhuyuan polymetallic deposit and its host granite, SE China. Geological Magazine 141, 225–231.

Li, C., Zhai, Q.G., Dong, Y.S., Huang, X.P., 2006. Discovery of eclogite and its geological significance in Qiangtang area, central Tibet. Chinese Science Bulletin 51, 1095–1100.

Li, H., Zhang, H., Ling, M.X., Wang, F.Y., Ding, X., Zhou, J.B., Yang, X.Y., Tu, X.L., Sun, W.D., 2011. Geochemical and zircon U–Pb study of the Huangmeijian A-type granite: implications for geological evolution of the Lower Yangtze River belt. International Geology Review 53, 499–525.

Li, S.M., Zhu, D.C., Wang, Q., Zhao, Z.D., Sui, Q.L., Liu, S.A., Liu, D., Mo, X.X., 2014. Northward subduction of Bangong–Nujiang Tethys: insight from Late Jurassic intrusive rocks from Bangong Tso in western Tibet. Lithos 205, 284–297.

Li, J.X., Qin, K.Z., Li, G.M., Richards, J.P., Zhao, J.X., Cao, M.J., 2014. Geochronology, geochemistry, and zircon Hf isotopic compositions of Mesozoic intermediate–felsic intrusions in central Tibet: petrogenetic and tectonic implications. Lithos 198, 77–91.

Li, G.M., Li, J.X., Zhao, J.X., Qin, K.Z., Cao, M.J., Evans, N.J., 2015. Petrogenesis and tectonic setting of Triassic granitoids in the Qiangtang terrane, central Tibet: evidence from U–Pb ages, petrochemistry and Sr–Nd–Hf isotopes. Journal of Asian Earth Sciences 105, 443–455.

Liu, M, 2012. Petrogenesis and Tectonic significance of early Jurassic alkalic Pluton in Nyainrong microcontinent, central Tibet. Unpublished Doctoral thesis, China University of Geosciences.

Liu, Y.S., Hu, Z.C., Gao, S., Gunther, D., Xu, J., Gao, C.G., Chen, H.H., 2008. In situ analysis of major and trace elements of anhydrous minerals by LA-ICP-MS without applying an internal standard. Chemical Geology 257, 34–43.

Liu, M., Zhao, Z.D., Guan, Q., Dong, G.C., Mo, X.X., Liu, Y.S., Hu, Z.C., 2011. Tracing magma mixing genesis of the middle Early-Jurassic host granites and enclaves in Nyanrong microcontinent, Tibet from zircon LA-ICP-MS dating and Hf isotopes. Acta Petrologica Sinica 27, 1931–1937.

Liu, D.L., Huang, Q.S., Fan, S.Q., Zhang, L.Y., Shi, R.D., Ding, L., 2014. Subduction of the Bangong–Nujiang Ocean: constraints from granites in the Bangong Co area, Tibet. Geological Journal 49, 188–206.

Liu, D.L., Shi, R.D., D, L., Huang, Q.S., Zhang, X.R., Yue, Y.H., Zhang, L.Y., 2015. Zircon U–Pb age and Hf isotopic compositions of Mesozoic granitoids in southern Qiangtang, Tibet: Implications for the subduction of the Bangong– Nujiang Tethyan Ocean. Gondwana Research http://dx.doi.org/10.1016/j.gr.2015.04.007 (in press).

Long, X.P., Wilde, S.A., Wang, Q., Yuan, C., Wang, X.C., Li, J., Jiang, Z.Q., Dan, W., 2015. Partial melting of thickened continental crust in central Tibet: Evidence from geochemistry and geochronology of Eocene adakitic rhyolites in the northern Qiangtang Terrane. Earth and Planetary Science Letters 414, 30–44.

Maniar, P.D., Piccoli, P.M., 1989. Tectonic discrimination of granitoids. Geological Society of America Bulletin 101, 635–643.

Martin, H., Smithies, R.H., Rapp, R., Moyen, J.F., Champion, D., 2005. An overview of adakite, tonalite–trondhjemite–granodiorite (TTG), and sanukitoid: relationships and some implications for crustal evolution. Lithos 79, 1–24.

McCarron, J.J., Smellie, J.L., 1998. Tectonic implications of fore-arc magnesian and generation of high-magnesian andesites: Alexander island, Antarctica. Journal of the Geological Society, London 155, 269–280.

Mckenzie, D., Bickle, M.J., 1988. The Volume and Composition of Melt Generated by Extension of the Lithosphere. Journal of Petrology 3, 625–679.

Middlemost, E.A.K., 1994. Naming materials in the magma igneous rock system. Earth-Science Reviews 37, 215–224.

Miyashiro, A., 1974. Volcanic rock series in island arcs and active continental margins. American Journal of Science 274, 321–355.

Murphy, M.A., Yin, A., Harrison, T.M., Dürr, S.B., Chen, Z., Ryerson, F.J., Kidd, W.S.F., Wang, X., Zhou, X., 1997. Did the Indo-Asian collision alone create the Tibetan plateau? Geology 25, 719–722.

Nelson, K.D., Zhao, W.J., Brown, L.D., Kuo, J., Che, J., et al., 1996. Partially molten middle crust beneath southern Tibet: synthesis of project INDEPTH results. Science 274, 1684–1688.

Pallares, C., Maury, R.C., Bellon, H., Royer, J.Y., Calmus, T., Aguillon-Robles, A., Cotten, J., Benoit, M., Michaud, F., Bourgois, J., 2007. Slab-tearing following ridge-trench collision: evidence from Miocene volcanism in Baja California, Mexico. Journal of Volcanology and Geothermal Research 161, 95–117.

Pan, G.T., Wang, L.Q., Li, R.S., Yuan, S.H., Ji, W.H., Yin, F.G., Zhang, W.P., Wang, B.D., 2012. Tectonic evolution of the Qinghai–Tibet Plateau. Journal of Asian Earth Sciences 53, 3–14.

Patiño Douce, A.E., 1999. What do experiments tell us about the relative contributions of crust and mantle to the origin of granitic magmas? Geological Society, London, Special Publications 168, 55–75.

Pearce, J.A., Stern, J.R., Bloomer, S.H., Fryer, P., 2005. Geochemical mapping of the Mariana arc–basin system: implications for the nature and distribution of subduction components. Geochemistry, Geophysics, Geosystems 6, Q07006. http://dx.doi.org/10.1029/2004GC000895.

Peng, T.P., Zhao, G.C., Fan, W.M., Peng, B.X., Mao, Y.S., 2015. Late Triassic granitic magmatism in the Eastern Qiangtang, Eastern Tibetan Plateau: geochronology, petrogenesis and implications for the tectonic evolution of the Paleo-Tethys. Gondwana Research 27, 1494–1508.

Plank, T., 2005. Constraints from thorium/lanthanumon sediment recycling at subduction zones and the evolution of the continents. Journal of Petrology 46, 921–944.

Plank, T., Langmuir, C.H., 1998. The chemical composition of subducting sediment and its consequences for the crust and mantle. Chemical Geology 145, 325–394.

Pullen, A., Kapp, P., Gehrels, G.E., Ding, L., Zhang, Q., 2011. Metamorphic rocks in central Tibet: lateral variations and implications for crustal structure. Geological Society of America Bulletin 123, 585–600.

Ramos, V.A., Folguera, A., 2009. Andean flat-slab subduction through time. Geological Society, London, Special Publications 327, 31–54.

Rapp, R.P., Watson, E.B., 1995. Dehydration melting of metabasalt at 8–32 kbar implications for continental growth and crust–mantle recycling. Journal of Petrology 38, 891–931.

Rogers, G., Saunders, A.D., Terrell, D.J., Verma, S.P., Marriner, G.F., 1985. Geochemistry of Holocene volcanic rocks associated with ridge subduction in Baja California, Mexico. Nature 315, 389–392.

Rudnick, R.L., Fountain, D.M., 1995. Nature and composition of the continental crust: a lower crustal perspective. Reviews of Geophysics 33, 267–309.

Rudnick, R.L., Gao, S., 2003. Composition of the continental crust. Treatise on Geochemistry 3, 1–64.

Sato, M., Shuto, K., Nohara-Imanaka, R., Takazawa, E., Osanai, Y., Nakano, N., 2014. Repeated magmatism at 34 Ma and 23-20 Ma producing high magnesian adakitic andesites and transitional basalts on southern Okushiri Island, NE Japan arc. Lithos 205, 60–83.

Saunders, A.D., Rogers, G., Marriner, G.F., Terrell, D.J., Verma, S.P., 1987. Geochemistry of Cenozoic volcanic rocks, Baja California, Mexico: implications for the petrogenesis of post-subduction magmas. Journal of Volcanology and Geothermal Research 32, 223–245.

Shi, R.D., Griffin, W.L., O'Reilly, S.Y., Huang, Q.S., Zhang, X.R., Liu, D.L., Zhi, X.C., Qiong, X.X., Ding, L., 2012. Melt/mantle mixing produces podiform chromite deposits in ophiolites: implications of Re–Os systematics in the Dongqiao Neo-tethyan ophiolite, northern Tibet. Gondwana Research 21, 194–206.

Sláma, J., Kosler, J., Condon, D.J., Crowley, J.L., Gerdes, A., Hanchar, J.M., Horstwood, M.S.A., Morris, G.A., Nasdala, L., Norberg, N., Schaltegger, U., Schoene, B., Tubrett, M.N., Whitehouse, M.J., 2008. Ple šovice zircon—a new natural reference material for U–Pb and Hf isotopic microanalysis. Chemical Geology 249, 1–35.

Smithies, R.H., Champion, D.C., 2000. The Archaean high-Mg diorite suite: links to tonalite–trondhjemite–granodiorite magmatism and implications for Early Archaean crustal growth. Journal of Petrology 41, 1653–1671.

Streck, M.J., Leeman, W.P., Chesley, J., 2007. High-magnesian andesite from Mount Shasta: a product of magma mixing and contamination, not a primitive mantle melt. Geology 35, 351–354.

Sun, S.S., McDonough, W.F., 1989. Chemical and isotopic systematics of oceanic basalts: implications for mantle composition and processes. In: Saunders, A.D., Norry, M.J. (Eds.), Magmatism in Ocean Basins. Geological Society of London. Special Publications 42, pp. 313–345.

Tapponnier, P., Zhiqin, X., Roger, F., Meyer, B., Arnaud, N., Wittlinger, G., Jingsui, Y., 2001. Oblique stepwise rise and growth of the Tibet plateau. Science 294, 1671–1677.

Tatsumi, Y., 2006. High-Mg andesites in the Setouchi volcanic belt, southwestern Japan: analogy to Archean magmatism and continental crust formation? Annual Review of Earth and Planetary Sciences 34, 467–499.

Tatsumi, Y., Eggins, S., 1995. Subduction Zone Magmatism. Blackwell, Cambridge (211 pp.).

Tatsumi, Y., Hanyu, T., 2003. Geochemical modeling of dehydration and partial melting of subducting lithosphere: toward a comprehensive understanding of high-Mg andesite formation in the Setouchi volcanic belt, SW Japan. Geochemistry, Geophysics, Geosystems 4, 1081.

Tiepolo, M., Tribuzio, R., 2008. Petrology and U–Pb zircon geochronology of amphibolerich cumulates with sanukitic affinity from Husky Ridge (Northern Victoria Land, Antarctica): insights into the role of amphibole in the petrogenesis of subduction-related magmas. Journal of Petrology 49, 937–970.

Wang, Q., Li, Z.X., Chung, S.L., Wyman, D.A., Sun, Y.L., Zhao, Z.H., Zhu, Y.T., Qiu, H.N., 2011. Late Triassic high-Mg andesite/dacite suites from northern Hohxil, North Tibet: Geochronology, geochemical characteristics, petrogenetic processes and tectonic implications. Lithos 126, 54–67.

Wang, X.-C., Li, Z.-X., Li, J., Pisarevsky, S.A., Wingate, M.T.D., 2014. Genesis of the 1.21 Ga Marnda Moorn large igneous province by plume–lithosphere interaction. Precambrian Research 241, 85–103.

Wang, B.D., Wang, L.Q., Chung, S.L., Chen, J.L., Yin, F.G., Liu, H., Li, X.B., Chen, L.K., 2016. Evolution of the Bangong–Nujiang Tethyan ocean: Insights from the geochronology and geochemistry of mafic rocks within ophiolites. Lithos 245, 18–33.

Wang, X.-C., Wilde, S.A., Li, Q.-L., Yang, Y.-N., 2016. Continental flood basalts derived from the hydrous mantle transition zone. Nature Communications 6, 7700.

Woodhead, J.D., Eggins, S.M., Johnson, R.W., 1998. Magma genesis in the New Britain Island Arc: further insights into melting and mass transfer processes. Journal of Petrology 39, 1641–1668.

Woodhead, J.D., Hergt, J.M., Davidson, J.P., Eggins, S.M., 2001. Hafnium isotope evidence for 'conservative' element mobility during subduction zone processes. Earth and Planetary Science Letters 192, 331–346.

Xu, R.H., Schärer, U., Allègre, C.J., 1985. Magmatism and metamorphism in the Lhasa block (Tibet): a geochronological study. Journal of Geology 93, 41–57.

Yin, A., Harrison, T.M., 2000. Geologic evolution of the Himalayan–Tibetan orogen. Annual Review of Earth and Planetary Sciences 28, 211–280.

Zeng, M., Zhang, X., Cao, H., Ettensohn, F.R., Cheng, W., Lang, X., 2015. Late Triassic initial subduction of the Bangong- Nujiang Ocean beneath Qiangtang revealed: stratigraphic and geochronological evidence from Gaize, Tibet. Basin Research 28, 147–157.

Zhai, Q.G., Jahn, B.M., Zhang, R.Y., Wang, J., Su, L., 2011a. Triassic subduction of the Paleo-Tethys in northern Tibet, China: evidence from the geochemical and isotopic characteristics of eclogites and blueschists of the Qiangtang Block. Journal of Asian Earth Sciences 42, 1356–1370.

Zhai, Q.G., Zhang, R.Y., Jahn, B.M., Li, C., Song, S.G., Wang, J., 2011b. Triassic eclogites from central Qiangtang, northern Tibet, China: petrology, geochronology and metamorphic P–T path. Lithos 125, 173–189.

Zhai, Q.G., Jahn, B.M., Su, L., Wang, J., Mo, X.X., Lee, H.Y., Wang, K.L., Tang, S.H., 2013. Triassic arc magmatism in the Qiangtang area, northern Tibet: zircon UPb ages, geochemical and Sr–Nd–Hf isotopic characteristics, and tectonic implications. Journal of Asian Earth Sciences 63, 162–178.

Zhang, K.J., Zhang, Y.X., Tang, X.C., Xia, B., 2012. Late Mesozoic tectonic evolution and growth of the Tibetan plateau prior to the Indo-Asian collision. Earth-Science Reviews 114, 236–249.

Zhang, K.J., Xia, B., Zhang, Y.X., Liu, W.L., Zeng, L., Li, J.F., Xu, L.F., 2014a. Central Tibetan Meso-Tethyan oceanic plateau. Lithos 210, 278–288.

Zhang, X.Z., Dong, Y.S., Li, C., Deng, M.R., Zhang, L., Xu, W., 2014b. Tectonic setting and petrogenesis mechanism of Late Triassic magmatism in Central Qiangtang, Tibetan Plateau: Take the Xiangtaohu pluton in the Hongjishan region as an example. Acta Petrologica Sinica 30, 547–564.

Zhu, D.C., Zhao, Z.D., Niu, Y.L., Mo, X.X., Chung, S.L., Hou, Z.Q., Wang, L.Q., Wu, F.Y., 2011. The Lhasa Terrane: record of a microcontinent and its histories of drift and growth. Earth and Planetary Science Letters 301, 241–255.

Zhu, D.C., Zhao, Z.D., Niu, Y.L., Dilek, Y., Hou, Z.Q., Mo, X.X., 2013. The origin and pre-Cenozoic evolution of the Tibetan Plateau. Gondwana Research 23, 1429–1454.